Structural, Magnetic and Optical Studies of the Polymorphic 9′-Anthracenyl Dithiadiazolyl Radical

Yassine Beldjoudi,[a†] Ana Arauzo,[b] Javier Campo,[b] Emma L. Gavey,[c] Melanie Pilkington[c] Mitchell A. Nascimento[a] and Jeremy M. Rawson*[a]

[a] Department of Chemistry & Biochemistry, University of Windsor, 401 Sunset Avenue, Windsor, ON, N9B 3P4, Canada. E-mail: jmrawson@uwindsor.ca
[b] Departamento de Física de la Materia Condensada, Facultad de Ciencias, and Instituto de Ciencia de Materiales de Aragon, CSIC-Universidad de Zaragoza, E-50009 Spain.
[c] Department of Chemistry, Brock University, 500 Glenridge Avenue, St. Catharines, Ontario L2S 3A1, Canada

Supporting Information Placeholder

ABSTRACT: The fluorescent 9′-anthracenyl-functionalized dithiadiazolyl radical (**3**) exhibits four structurally determined crystalline phases, all of which are monomeric in the solid-state. Polymorph **3α** (monoclinic $P2_1/c$, $Z' = 2$) is isolated when the radical is condensed onto a cold substrate (enthalpically favored polymorph) whereas **3β** (orthorhombic $P2_12_12_1$, $Z' = 3$) is collected on a warm substrate (entropically favored polymorph). The **α** and **β** polymorphs exhibit chemically distinct structures with **3α** exhibiting face-to-face π–π interactions between anthracenyl groups while **3β** exhibits edge-to-face π–π interactions. **3α** undergoes an irreversible conversion to **3β** on warming to 120 °C (393 K). The β-phase undergoes a series of reversible solid-state transformations on cooling; below 300 K a phase transition occurs to form **3γ** (monoclinic $P2_1/c$, $Z' = 1$) and on further cooling below 165 K a further transition is observed to **3δ** (monoclinic $P2_1/n$, $Z' = 2$). Both **3β → 3γ** and **3γ → 3δ** transitions are reversible (single-crystal X-ray diffraction) and the **3γ → 3δ** process exhibits thermal hysteresis with a clear feature observed by heat capacity measurements. Heating **3β** above 160 °C generates a fifth polymorph (**3ε**) which is distinct from **3α – 3δ** based on PXRD data. The magnetic behavior of both **3α** and the **3β/3γ/3δ** system reflect an S = ½ paramagnet with weak antiferromagnetic coupling. The reversible 3**δ** ↔ 3**γ** phase transition exhibits thermal hysteresis of 20 K. Below 50 K the value of $\chi_m T$ for **3δ** approaches 0 emu·K·mol^{-1} consistent with formation of a gapped state with an S = 0 ground state configuration. In solution both paramagnetic **3** and diamagnetic [**3**][$GaCl_4$] exhibit similar absorption and emission profiles reflecting similar absorption and emission mechanisms for paramagnetic and diamagnetic forms. Both emit in the deep-blue region of the visible spectrum ($\lambda_{em} \sim 440$ nm) upon excitation at 255 nm with quantum yields of 4% (**3**) and 30% ([**3**][$GaCl_4$]) affording a switching ratio [$\Phi_F(\mathbf{3}^+)/\Phi_F(\mathbf{3})$] of 7.5 in quantum efficiency with oxidation state. Solid-state films of both **3** and [**3**][$GaCl_4$] exhibit emission bands at longer wavelength (490 nm) attributed to excimer emission.

Introduction

Over the last few decades, molecule-based organic materials have emerged as attractive building blocks for a diverse range of applications from OFET[1] and OLED[2] devices through to molecular conductors[3] and magnets[4] *inter alia*. In particular, the soft nature of these molecular solids in relation to conventional ceramics makes them particularly sensitive to molecular deformations which can be driven by relatively mild thermal[5]- or pressure[6]-induced changes or by light.[7] These changes in physical response are often associated with small atomic displacements and sometimes occur reversibly through single-crystal-to-single-crystal transformations. Such structural changes can lead to subtle or more dramatic effects in the physical response, whether it be optical, magnetic or electronic.[8] The incorporation of two (or more) physical properties into the same system can lead to multi-functional materials in which the two types of behavior interact either independently of or cooperatively with each other. In many cases paramagnetism and emission can be considered antagonistic rather than complimentary properties with free radicals often leading to emission quenching.[9] However recent work has proposed that open shell molecules can provide a route to OLED device fabrication with emission quantum yields up to 100%.[10] In the current manuscript we describe the synthesis and characterization of a main group radical covalently attached to an organic fluorophore and examine its electronic and optical properties in solution and polymorphism as well as single-crystal-to-singe-crystal transitions in the solid state.

Although there are many groups of stable radicals,[11] one particular group of compounds which exhibit a rich tapestry of solid-state phase transitions are the family of thiazyl radicals comprising π-conjugated C/N/S rings such as the 1,2,3- and 1,3,2-dithiazolyls (DTA) and 1,2,3,5-dithiadiazolyls (DTDA) (Scheme 1). These radicals have given rise to some of the highest magnetic ordering temperatures known for organic magnets,[12,13] and whose magnetic and conducting properties change under pressure. In addition these systems have been shown to exhibit a photo-conducting response.[14] Other thiazyl radicals undergo reversible spin-pairing, exhibiting both diamagnetic and paramagnetic phases which can be interconverted by heat, light and pressure.[7b,15] For DTDA radicals the paramagnetism is typically quenched through formation of a set of multi-center π–π

bonding interactions. These comprise intermolecular contacts substantially shorter than the sum of the van der Waals' radii and an eclipsed geometry rather than staggered conformation typical of π-π interactions in graphite. These unusually close contacts were first described as "pancake bonds" by Mulliken and Person,[16] a term which has received a recent resurgence.[17] The multicenter bonding nature of the orbital interaction was identified by Banister among others during structural studies on dimers of DTDA and $S_3N_2^{+\bullet}$radicals.[18] More recent work by Miller and Novoa have described these types of interactions between radicals as 'long distance bonds'.[19] In a number of instances such π-stabilized radicals can alternatively adopt reversible 2*c*,2*e*- σ- bond formation in which the loss of π-delocalization is compensated by the strength of a localized E-E σ-bond.[15b,20]

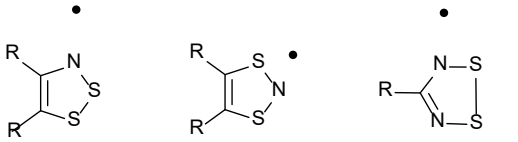

1,2,3-DTA 1,3,2-DTA 1,2,3,5-DTDA

Scheme 1. Selected stable thiazyl radicals

One of the most studied of these families of radicals is the 1,2,3,5-dithiadiazolyl (DTDA) radical which has been explored as a building block in the field of organic radical conductors, exhibiting conductivities[21] up to 10^2 S/cm and as building blocks in the design of some of the highest T_C organic magnets,[12] as paramagnetic ligands in coordination chemistry[22] and as photo-conducting materials.[14] Electrochemical,[23] EPR and spin density studies[24] have shown that the singly occupied molecular orbital (SOMO) of the DTDA ring is localised on the S/N ring and to a good approximation the R group (Scheme 1) can be modified without change to the electronics of the DTDA ring. Previous work has focused on the ability to tailor the R substituent in order to modify the solid state packing and the resultant solid state properties.[25] As part of our recent development of multi-functional DTDA radicals we have examined R groups which bring additional functionality to the system and recently reported the blue-emitting fluorescent radicals **1** and **2** (Scheme 2).[26,27] Here the emission profile of both the radical (e.g. **2**) and its diamagnetic analogue (e.g. $\mathbf{2}^+$) are essentially the same but the radical participates in enhancing non-radiative electronic relaxation leading to distinctly different quantum efficiencies between the radical and the corresponding diamagnetic cation; $\Phi_F(\mathbf{1}^+)/\Phi_F(\mathbf{1})$ = 3 whereas $\Phi_F(\mathbf{2}^+)/\Phi_F(\mathbf{2})$ = 2 offering future opportunities for attenuation of emission through redox switching. In the solid state we found that the wavelength of excitation affects the physical response of **2** with excitation at shorter wavelengths (375 nm) giving rise to excimer fluorescence whereas long wavelength excitation (455 nm) led to a marked photocurrent.[27]

As an extension of those initial studies we wished to prepare a poly-aromatic hydrocarbon (PAH) which contribute an optical response bonded to a DTDA radical in which dimerization is suppressed to retain paramagnetism in the solid state. As part of our design process we considered previous paramagnetic DTDA radicals and noted that the presence of CF_3 groups in the *ortho* positions in 2',4',6'-$(F_3C)_3C_6H_2CNSSN$ led to a large twist angle between aryl and DTDA rings suppressing the preferred cis-oid π*-π* dimerization.[28] Similarly the monomeric radicals *p*-XC_6F_4CNSSN, (X= CN, Br, NO_2, p-NCC_6F_4) have twist angles in the range 32 – 58° (mean 48°),[29-31] suggesting that the increase in steric bulk associated with increasing torsion angle suppresses dimerization. In this context we targeted the 9'-anthrcenyl radical, **3** which has the potential to combine the fluorescent properties of the anthracenyl group with the paramagnetic DTDA radical. A preliminary search of the CSD[32] for CN_2 fragments bound to the 9'-anthracenyl group revealed an average twist angle of 52° between the CN_2 plane and the anthracenyl group, which augered well for the common cis-oid dimerization process[33] to be suppressed in **3**. While *p*-NCC_6F_4CNSSN and 2,4,6-$(F_3C)_3C_6H_2CNSSN$ both retain their paramagnetism in the solid state and both exhibit two polymorphs,[28,34] we have found **3** not only retains its paramagnetism in the solid state but also exhibits a remarkably rich polymorphism. Despite its molecular rigidity (1 torsional degree of freedom) which suppresses conformational polymorphism,[35] **3** exhibits four structurally determined phases (**3α** – **3δ**). We examine the relative thermodynamic stability of the polymorphs **3α** – **3δ**, the irreversible transition **3α** →**3β** and probe the reversible nature of the phase transitions **3β** ↔ **3γ** ↔ **3δ** through variable temperature single crystal and powder X-ray diffraction, DSC and magnetic measurements.

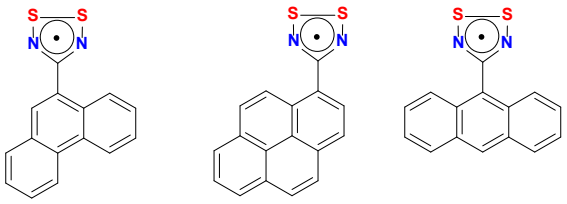

Scheme 2: Dual fluorophore-DTDA radical derivatives.

Results

The majority of DTDA radicals are prepared from the corresponding nitrile utilising a standard synthetic procedure.[36,37] This procedure proved ineffective for the synthesis of **3** due to the reduction of the anthracenyl functional group by $Li[N(SiMe_3)_2]$ affording a dark blue EPR active solution of the anthracene carbonitrile radical anion (Scheme S1 and Figure S4). To circumvent radical anion formation, **3** was prepared from the corresponding 9-bromo-anthracene (**4**) *via* lithium/halogen exchange, a procedure already reported in the literature,[27,28] followed by reaction with bis(trimethylsilyl)carbodiimide to generate the *N*-lithio salt of the amidinate. Subsequent condensation with SCl_2 afforded [**3**]Cl which was reduced using Ag powder in THF (Scheme 3) with crystals of **3** isolated by vacuum sublimation. Compound **3** crystallized in two different phases, **3α** and **3β**, depending on the sublimation conditions. When sublimed onto a water-cooled cold-finger (ca. 10 °C) a mixture of **3α** and **3β** was observed. Adjustment to these conditions afforded phase pure material. When sublimed onto a

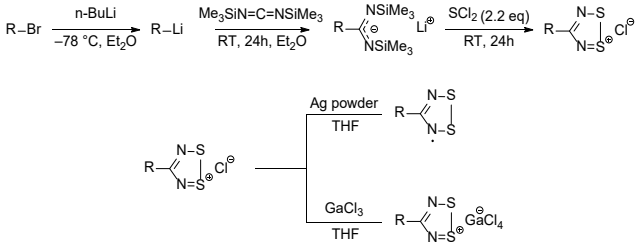

Scheme 3: Synthesis of **3** and [**3**][$GaCl_4$] (R = 9′-anthracenyl)

cold-finger maintained at -15 °C, **3α** was selectively obtained whereas pure **3β** was obtained when the substrate was maintained in the region 50 – 70 °C.

Previous studies on the polymorphism of DTDA radicals revealed that the temperature of the substrate can play a crucial role in determining the solid-state morphology.[34] Specifically when there are multiple minima on the potential energy hypersurface which are close in energy then subtle changes to the crystallization conditions (partial pressure temperature) can afford different polymorphs. In this context it is noteworthy that 2′,6′-$F_2C_6H_3CNSSN$ exhibits three polymorphs[38] and the completely rigid molecule ClCNSSN exhibits a remarkable five polymorphs,[39] all formed by vacuum sublimation.

Solution EPR and Electrochemical Studies: For **3** a typical 1:2:3:2:1 pentet was observed in the solution EPR spectrum (Figure S5). Electrochemical studies on **3** in solution revealed a reversible 1e^- oxidation to form **3**$^+$ with a redox potential ($E_{1/2}$ = +0.73 V *vs* Ag/AgCl, Figure S6) similar to other DTDA radicals.[23]

Spectroscopic Properties: All solution samples of **3** and [**3**][$GaCl_4$] for UV/vis and emission studies were measured under high dilution (<10^{-5} M). A solution UV/visible absorption spectrum of **3** (4 × 10^{-7} M in MeCN) revealed an absorption profile dominated by the anthracene functionality which exhibits well-structured sets of bands with a strong absorption at 255 nm, a set of weaker longer wavelength

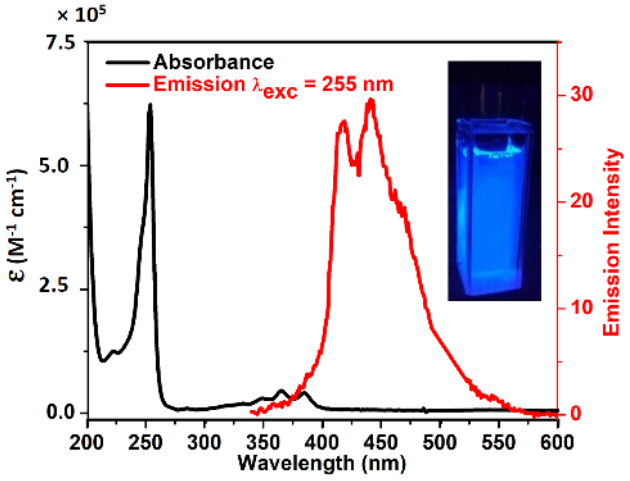

Figure 1. (black) Excitation profile of **3** which gives rise to emission at 440 nm; (red) emission profile of **3** on excitation at 255 nm. [4 × 10^{-7} M solution of **3** in MeCN)]. (inset) the fluorescence of **3** under UV irradiation (λ_{exc} = 255 nm).

absorptions in the range 340 – 390 nm and the absence of features around 450 – 500 nm which are associated with formation of pancake-bonded dimers (Figure 1).[40] Solution fluorescence studies on **3** revealed an intense emission at 440 nm (Figure 1, Figure S7). The results are summarized in Table S5. In order to understand the role of the unpaired electron on the optical properties of **3**, we examined the spectroscopic properties of the diamagnetic salt [**3**][$GaCl_4$] which was prepared from a 1:1 mixture of [**3**]Cl and $GaCl_3$ (Scheme 3). The salt [**3**][$GaCl_4$] exhibits essentially the same absorption and broad emission spectra as **3** (Figure S7) but with an enhanced quantum yield (Φ_F = 30 %, λ_{exc} = 255 nm). This behavior is analogous to our previous observations[26,27] on the closely related systems **1**$^+$/**1** and **2**$^+$/**2** which reflect (i) the largely innocent nature of the radical electron in the energetics of the excitation/emission process but (ii) does enhance non-radiative decay kinetics leading to decreases in quantum yield for the radical with respect to the diamagnetic cationic analogue. Although **3** and **3**$^+$ show lower quantum yields than **1**$^+$/**1** and **2**$^+$/**2** systems, a higher switching ratio was observed in solution (Φ_{3+}/Φ_3 = 7.5 at λ_{ex} = 255 nm *vs* 3 and 2 for **1**$^+$/**1** and **2**$^+$/**2** respectively).

Time-dependent DFT (UB3LYP/6-311G*+) gas phase calculations on the doublet radical **3** revealed the lowest energy absorption to be the α-HOMO → α-LUMO transition but this has an extremely small oscillator strength. Indeed the computed UV/vis profile reveals a dominant transition at 243 nm (oscillator strength, *f* = 3.437, Table S3), in reasonable agreement with the experimentally observed UV/visible absorption band around 255 nm in MeCN solution (Figure S13). Unlike conventional fluorophores based on diamagnetic (organic) molecules, the doublet nature of the spin ground state leads to components of the excitation spectrum derived from both α and β-spins (i.e. 'spin up' and 'spin down' electrons). The SOMO orbital from an RHF description of the electronic configuration translates to a linear combination of the α-HOMO and β-LUMO in the unrestricted model. An analysis of the transitions with large oscillator strengths reveals that none of these intense transitions involve the unpaired electron (α-HOMO) (Table S6), confirming the largely innocent nature of the radical electron in the absorption profile. However some components of the 243 nm transition have a charge-transfer contribution from the anthracenyl group to the DTDA moiety (Table S6). Indeed the emission profiles of **3** and **3**$^+$ are very similar indicating that both follow a similar mechanism but with more efficient non-radiative decay mechanisms for radical **3** reflected in a lower quantum yield. Previous excited state lifetime studies for **2** and **2**$^+$ (as representative of this family of radicals) revealed a single first order exponential decay curve with ca. 5 ns lifetime, indicative of a dominant fluorescence process.[27]

Spectroscopic properties of Thin Films of 3 and 3$^+$ in PMMA: Thin films were prepared by drop-casting CH_2Cl_2 solutions of **3** and [**3**][$GaCl_4$] with polymethyl methacrylate (PMMA) according to previous protocols.[26,27] The absorption spectra of **3**:PMMA and [**3**][$GaCl_4$]:PMMA composite films at 1:1000 *w/w* ratio were found to be similar to the solution spectra showing a strong absorption band at 257 nm and a lower intensity absorption band near the visible region (Figure S8). The corresponding emission bands are

centred at 420 nm (*cf* 440 nm in solution) and are attributed to the monomer emission of **3** and [**3**][$GaCl_4$] (Figure S9). The emission bands are similar to the solution emission spectra, indicating that at these low concentrations there is no evidence for aggregation.

Solid state spectroscopic properties of 3 and 3⁺: Anthracenes are susceptible to fluorescence quenching *via* photodimerization (4+4 cycloaddition, Scheme 4), e.g. methyl-anthracene-9-carboxylate undergoes photo-dimerization despite the anthracene rings being 3.9 – 4.4 Å apart.[42] In the context of the current studies, Yamada *et al*. described changes in the magnetic properties of anthracene-functionalized TEMPO radicals due to UV light-induced photo-dimerization.[43] Although **3α** exhibits the desired face-to-face conformation of anthracenyl groups with a separation of 3.39 Å appropriate for photodimerization,[44] photoexcitation of a single crystal of **3α** using 360 nm radiation for 7 days revealed no structural change (Table S1).

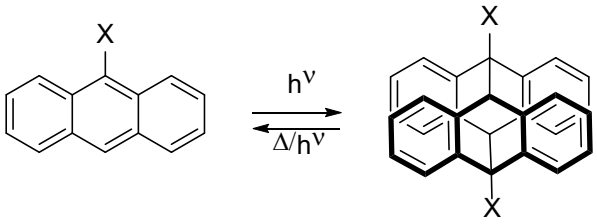

Scheme 4: [4+4] photo-reaction of anthracene

In the absence of photodimerization, we were able to pursue preliminary studies of the solid-state photo-luminescence of **3**. Thin films of **3** and [**3**][$GaCl_4$] were prepared by drop-casting solutions onto quartz slides under inert conditions. Their high surface area made these samples extremely air sensitive and it has not yet proved possible to determine the phase of **3** prepared under these conditions e.g. by PXRD studies. Since all structural phases of **3** identified to date are monomeric (*vide infra*), these films permitted us to establish whether the radical would quench emission in the solid state. Despite the presence of the unpaired electron in **3**, the emission spectra of pure solid films of **3** and [**3**][$GaCl_4$] display nearly identical emission spectra with a broad, featureless emission band at 490 nm and 480 nm respectively (Figure 2, Figure S10), significantly red-shifted with respect to dilute solutions and composite films, e.g. **3** emits at 420 and 440 nm in PMMA films and CH_2Cl_2 solution respectively but its solid state emission (Figure 2) at 490 nm is consistent with excimer formation.[45]

The luminescence of anthracene is deeply influenced by the molecular solid-state packing. Previous studies have reported that the slipped *π-stacked* arrangement of anthracene molecules (which offers a weak π–π interaction) show monomer emission, whereas the *zig-zag* arrangement of molecules interacting *via edge-to-face* π–π interactions displays excimer emission.[46-48] Conversely, recent studies on a polymorphic anthracene derivative revealed high-efficiency excimer green fluorescence (Φ_{PL} = 76.8%) when anthracene moieties interact *via face-to-face* interactions whereas *edge-to-face* interactions in the second polymorph, offered blue emission (Φ_{PL} = 8.1%).[49] Given the complexity of anthracene emission, we can only comment at this time

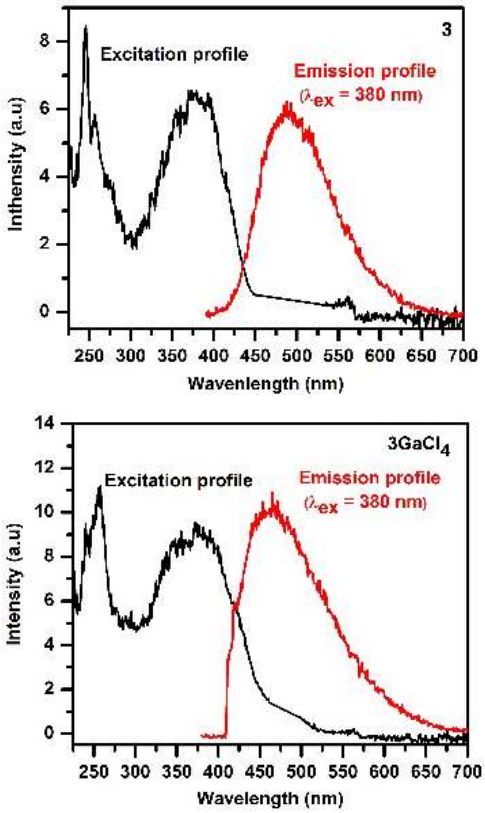

Figure 2: Solid-state excitation profile (black) and emission (red) profiles measured on thin films of (top) **3** and (bottom) [**3**][$GaCl_4$].

that the retention of paramagnetism in the solid state appears not to quench emission in **3**.

Crystallographic studies: Radical **3** is polymorphic and crystallises in either of two polymorphs, depending upon sublimation conditions. Polymorph **3α** crystallises when **3** is sublimed onto a cold finger maintained at -15 °C (enthalpically favoured polymorph) whereas polymorph **3β** is formed on a warmer substrate (+50 °C) (entropically favoured polymorph). The structure of **3α** does not display any thermally-induced structural modifications on cooling (Table S1) but undergoes an irreversible phase transition to **3β** upon warming (*vide infra*). Polymorph **3β** undergoes several reversible phase transitions to **3γ** and then **3δ** upon cooling associated with subtle changes in the periodicity of the $^{\delta+}S\cdots N^{\delta-}$ and anthracenyl *edge-to-face* C-H···π intermolecular contacts common to this set of structures. The reversibility of these phase transitions has been confirmed through magnetic measurements, variable temperature PXRD studies and differential scanning calorimetry. Crystallographic data for **3α** – **3δ** are summarized in Table 1 with more detailed temperature dependent studies reported in Tables S2 and S3. A brief description of each structure is presented below and the subsequent Discussion section discusses the polymorphic behaviour in more detail.

Crystal structure of 3α: Polymorph **3α** adopts the monoclinic space group $P2_1/c$) with one molecule in the asymmetric unit. Radical **3α** does not exhibit the classical *cis*-oid 'pancake' bond typical of most DTDA radicals.[17] The C-H

bonds at the 1′ and 8′ positions on the anthracenyl substituent ring place H atoms close to the DTDA ring and these are accommodated by a large twist angle (73.22° at 150 K) between the DTDA and polyaromatic hydrocarbon (PAH) rings. Twist angles of this size have been previously observed when positioning bulky groups at the *ortho* position of the phenyl ring in 2,4,6-$(F_3C)_3C_6H_2CNSSN$ (θ = 69 – 87°).[28] A pair of these radicals form classical van der Waals π–π interactions between the PAH rings (Figure 3a) with the anthracenyl rings displaced so that the C atoms are located over the centroid of a neighbouring ring with closest C···C contacts in the range 3.388(6) – 3.393(5) Å, comparable to those found in graphite (3.35 Å).[50] Anthracene derivatives exhibiting similar π–π interactions have been reported previously albeit with slightly longer contacts (> 3.565(2) Å) than those of **3α**.[51] The structure of **3** in **3α** exhibits a marked *out-of-plane* bending of the C-C bond linking the anthracenyl and DTDA rings by ~8° and is not observed in other polymorphs of **3**, although marked distortions of this type have been observed in diselenadiazolyl chemistry in which bending occurs among a series of $(p\text{-}RC_6F_4CNSeSeN)_2$ dimers in order to maximize pancake bonding.[52] In the current case this distortion could be to form (i) additional C-H···N hydrogen bonds from the 10′ position of the anthracene ring and the DTDA N atom (C-H···N 2.74 Å, C-Ĥ···N = 132.1°) (Figure 3a) which augment the π–π interactions between anthracenyl rings and/or (ii) maximizing "SN-IV" type intermolecular interactions[25] between radicals with $^{\delta+}S\cdots N^{\delta-}$ contacts of 2.876(3) and 3.129(3) Å (Table 2). The

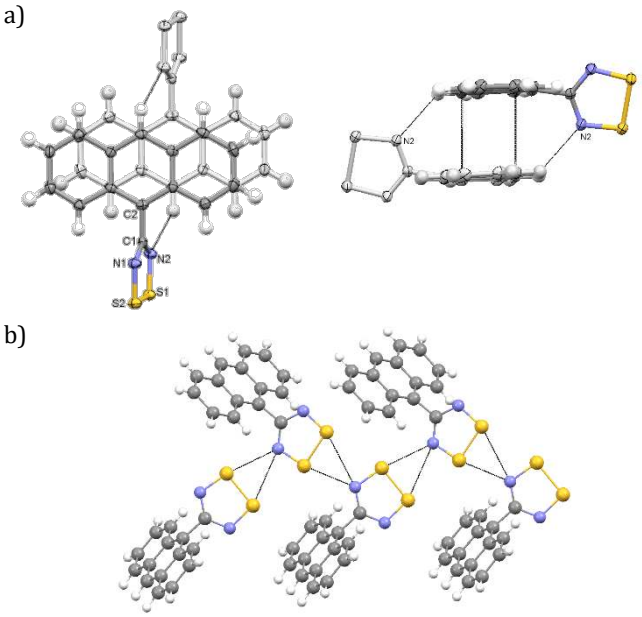

Figure 3: The crystal structure of **3α**: (a) Two views of the centrosymmetric dimer formed via π–π interaction between PAH rings and C-H···N contacts (coloured molecule at *x*, *y*, *z* and the symmetry-related monochrome molecule related *via* the symmetry operator 1 – *x*, 1 – *y*, 2 – *z*); (b) Propagation of $^{\delta+}S\cdots N^{\delta-}$ contacts along the crystallographic *b*-axis.

Table 1. Summary of crystallographic data for the four polymorphs of 3.

Parameters	Phase			
	α	β	γ	δ
Formula	$C_{15}H_9N_2S_2$	$C_{15}H_9N_2S_2$	$C_{15}H_9N_2S_2$	$C_{15}H_9N_2S_2$
FW	281.36	281.36	281.36	281.36
Temp. (K)	150(2)	310(2)	173(2)	150(2)
Crystal system	Monoclinic	Orthorhombic	Monoclinic	Monoclinic
Space group	$P2_1/c$	$P2_12_12_1$	$P2_1/c$	$P2_1/n$
a/Å	10.2054(3)	10.7397(13)	14.7027(11)	13.4489(13)
b/Å	7.9074(2)	14.859(2)	10.7141(7)	14.7539(15)
c/Å	15.6084(4)	24.974(3)	8.2871(5)	13.4607(13)
α/°	90	90	90	90
β/°	100.069(1)	90	98.771(4)	104.725(3)
γ/°	90	90	90	90
V/Å^3	1240.17(6)	3985.5(9)	1290.17(15)	2583.1(4)
Z	4	12	4	8
Dc/Mg m^{-3}	1.507	1.407	1.449	1.447
Unique reflns	2421	8116	2090	3872
Reflns [I>2σ(I)]	1983	4988	1601	3338
R_{int}	0.09	0.069	0.093	0.092
S	1.12	1.05	1.05	1.07
R_1 (I> 2σ(I))	0.087	0.092	0.086	0.055
wR_2 (all)	0.239	0.243	0.231	0.151
$\Delta\rho_{max}$, $\Delta\rho_{min}$ (e Å^{-3})	0.70, -0.66	0.65, -0.56	0.72, -0.48	0.39, -0.38

Table 2: Selected crystallographic parameters for the different polymorphs of **3**

Polymorph	Temp (K)	Anthracene-DTDA Torsion angle (°)	SN-IV S···N contacts (Å)	C-H...π *edge-to-face* interactions (Å)	C-H...π angle (°)	Angle between anthracene ring planes (°)
α	150	73.22	2.876(3), 3.129(3)	/	/	/
β	310	79.06, 82.74, 86.04	2.86(1) – 3.06(1) (mean 2.96)	2.96 – 3.14 (mean 3.03)	163.43 – 174.90 (mean 168.96)	72.26, 72.38, 72.25 (mean 72.30)
γ	173	75.06	2.844(5), 3.014(5) (mean 2.929)	2.983 – 3.039 (mean 3.009)	164.70 – 165.05 (mean 164.84)	72.33
δ	150	72.52, 75.66	2.784(4)–3.065(4) (mean 2.933)	2.738 – 2.836* (mean 2.777)	164.01 – 165.87* (mean 164.91)	69.93

* only 50% of the anthracenyl functional groups afford an edge to face C-H···$\pi_{centroid}$ interaction in the **3δ** phase.

latter propagate parallel to the crystallographic *b*-axis (Figure 3b). These SN-IV interactions are analogous to those observed for previously reported PAH-DTDA derivatives, **1** and **2**.[26,27] The structure of **3α** can therefore be considered as a two-dimensional sheet with chains of radicals linked along the crystallographic *b*-axis and then each chain cross-linked to neighbouring chains *via* π–π interactions. The structure of **3α** was also measured at 280 K and displays a slight lattice expansion with a slight increase of the $S^{\delta+}...N^{\delta-}$ distances (2.934(6) and 3.150(5) Å) compared to the low temperature structure determination (Table S4).

Crystal structure of 3β : Crystals of **3β** could be selectively grown by sublimation onto a warm substrate (50 – 70 °C). Polymorph **3β** undergoes a reversible phase transition to form **3γ** upon cooling below 300 K (27 °C) and the closeness of the phase transition to ambient temperature tended to lead to poorer crystallinity upon prolonged storage. A crystal structure of **3β** was determined at 310 K (i.e. near the phase transition) (Table 1) and additional measurements were made at higher temperatures (330 and 360 K, Table S2), further from the transition temperature. Apart from small changes to the intermolecular contacts and anticipated unit cell expansion upon warming there were no significant changes. Of these the structure determination at 310 K is described here.

Polymorph **3β** crystallises in the orthorhombic space group $P2_12_12_1$ with three molecules in the asymmetric unit. The twist angle between the DTDA and anthracene rings is larger (79.06 – 86.04 °, mean 82.61°) than that observed in **3α** (73.21°) (Table 2). The radicals in **3β** also retain their monomeric nature in the solid state. Like **3α**, the structure of **3β** exhibits SN-IV type contacts leading to formation of supramolecular chains (Figure 4a), Unlike **3α** where there is one molecule in the asymmetric unit and a regular chain, the presence of three molecules in the asymmetric unit leads to three sets of crystallographically independent SN-IV contacts in **3β** forming an irregular chain structure parallel to the crystallographic *c*-axis. The intermolecular $^{\delta+}S\cdots N^{\delta-}$ contacts are in the range of 2.86(1) – 3.05(1) Å. Perpendicular to this each anthracene molecule forms a set of three C-H···π *edge-to-face* interactions. These are well established interactions in anthracene chemistry and indeed common for polyacenes in general.[46] Each crystallographically distinct molecule forms three C-H···$\pi_{centroid}$ interactions to a neighbouring anthracenyl group with C-H···$\pi_{centroid}$ distances in the range 2.96 – 3.14 Å (Table 2, Figure 4d) and C-H...$\pi_{centroid}$ angles which are nearly linear (mean 168°). The two anthracene rings involved in each of these interactions form angles of *ca*. 72° (Table 2).

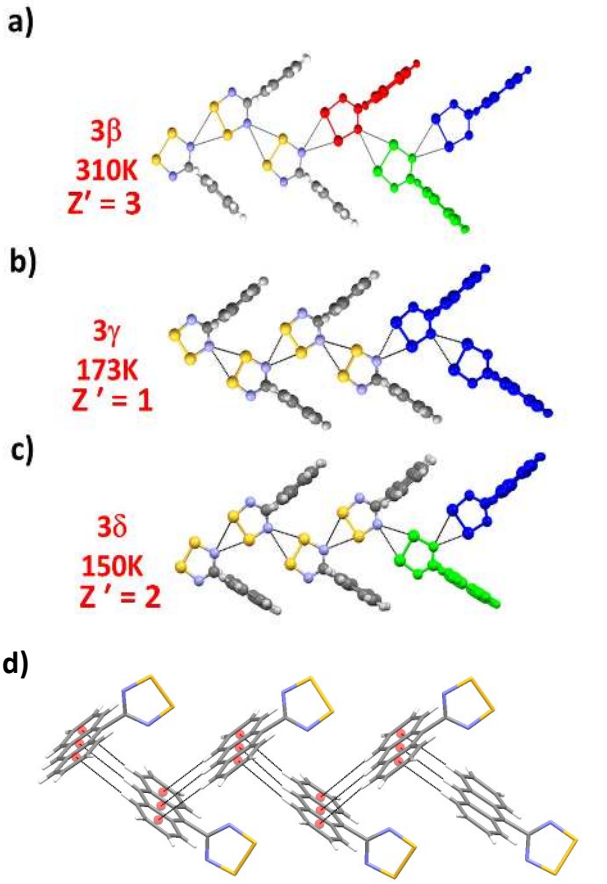

Figure 4: The crystal structures of (a) **3β**, (b) **3γ** and (c) **3δ** showing propagation of the SN-IV contacts and highlighting the crystallographically independent molecules; (d) Propagation of *edge-to-face* C-H···π interactions in **3β** (red circles represent ring centroids).

Crystal structure of 3γ: Cooling **3β** below 300 K leads to a transition to polymorph **3γ** which crystallizes in the monoclinic space group $P2_1/c$ with one molecule in the asymmetric unit. The relationship between **3γ** and **3β** is essentially a symmetry lowering from orthorhombic (Z′ = 3) to monoclinic (Z′ = 1) on cooling. This structural transition is coupled with a *ca*. three-fold decrease in the *c*-axis from 24.974(3) to 8.2871(5) Å (Figure S1) and a switching of *a* and *b* axes. At 173 K the twist angle between the DTDA and anthracenyl rings in the one crystallographically unique molecule is still large (75.06°) but closer to that observed in **3α** (73.22°) than in **3β** (79.06 – 86.04°).

The network of intermolecular contacts in **3γ** is otherwise very similar to **3β** with molecules linked *via* SN-IV type interactions ($d_{S\cdots N}$ = 2.843(5) and 3.014(5) Å) forming a uniform, regularly spaced chain parallel to the crystallographic *c*-axis (Figure 4b). These chains are linked *via* edge-to-face C-H···π interactions analogous to those in **3β** (Figure S2). The C-H···$\pi_{centroid}$ distances in **3γ** are in the range 2.98 – 3.04 Å similar to **3β** and the angle formed between anthracene units (72.29°) is almost identical to those observed for **3β** (mean 72.30°, Table 2) The average C-H···$\pi_{centroid}$ angle is 165° suggesting a more marked deformation from ideality (180°) when compared to **3β** (169°).

***Crystal structure of 3δ*:** Polymorph **3δ** was formed by cooling **3γ** below 165 K and crystallizes in the monoclinic space group $P2_1/n$ with two molecules in the asymmetric unit. Again **3δ** is monomeric with a large twist angle between the DTDA and anthracenyl planes for each of the two crystallographically independent molecules (~72.52° and 75.66°) and comparable to **3α**, **3β** and **3γ** (Table 2). Like all other forms of **3**, **3δ** exhibits a set of SN-IV type intermolecular $S^{\delta+}\ldots N^{\delta-}$ contacts. In **3δ** these contacts alternate forming sets of short and long distances (Figure 4c). The S···N distances range from 2.784(4) – 3.065(4) Å and are the shortest compared to all the other polymorphs (Table S4). While these interactions propagate parallel to the crystallographic *c*-axis in both **3β** and **3γ**, these interactions propagate along a unit cell diagonal in **3δ**, making the correspondence between **3δ** and **3β**/**3γ** phases more challenging.

With two molecules in the asymmetric unit there are two sets of C-H···π interactions. In **3δ**, one set of interactions is the classical set of three C-H···$\pi_{centroid}$ contacts (analogous to those shown in Figure 4d) although the C-H···$\pi_{centroid}$ interactions (2.74 – 2.84 Å, Table 2) are shorter than in both **3β** and **3γ**. In contrast the second set of interactions shows a distinct lateral slippage of the two anthracene rings with respect to each other such that the C-H bonds are now oriented towards the C-C bonds of the central C_6-ring rather than the ring centroid (Figure S3). This is reflected in the C-H···$\pi_{centroid}$ angles (mean 162.60°) which clearly reflect a significant displacement of the two anthracenyl rings and a move from C-H···$\pi_{centroid}$ to C-H···π_{edge}. The resulting C-H···π interaction to the midpoint of the C-C bond is reflected in C-H···π_{edge} distances of 2.92 and 3.10 Å with corresponding C-H···π_{edge} angles of 172.38 and 174.30°.

Thermal studies of polymorphism in 3:

Polymorphism occurs because different crystalline packing arrangements can result in near equi-energetic free energies.[53] In the case of **3**, there is only one torsional degree of freedom, i.e. the twist angle between DTDA and anthracenyl ring planes. Among the polymorphs **3α** – **3δ** only a small structural variation is observed in these torsion angles (73 – 83°, Table 2) precluding the presence of conformational isomerism.[35] The differences observed within this series of structures merely reflect differences in molecular packing. The isolation of different polymorphs of 3 arises from subtle differences in crystallization conditions (temperature, pressure etc). The current system is particularly intriguing in this aspect as it provides examples of both enantiotropic polymorphs (reversible transitions can occur between polymorphs before the melting point) and monotropic polymorphs in which the transition is irreversible. Since both **3α** and **3β** could be grown selectively by controlling sublimation conditions, these two polymorphs provided the starting point for variable temperature studies.

Monotropic polymorphism: The transformations 3α → 3β → 3ε: Variable temperature powder X-ray diffraction (VT-PXRD) studies on **3α** revealed it is thermally stable to 100 °C (Figure 5) but heating above 120 °C led to marked changes in the powder pattern (e.g. significantly increased intensities of reflections around 11.5 and 19.5° and decreases in features at 12.5 and 18.5°). Analysis of the PXRD pattern after heating **3α** to 120 °C confirmed it to be **3β** (PXRD profiles for both **3α** and **3β** along with their simulations are provided as supporting information, Figure S17). There was no significant change in PXRD pattern after cooling back to room temperature, consistent with monotropic polymorphism in which there is irreversible conversion of **3α** to **3β** upon heating. Notably further heating of **3β** to temperatures in excess of 160 °C led to a further irreversible change and the emergence of another polymorph (**3ε**) whose PXRD profile is distinct from **3α** and **3β**. After cooling from 200 °C to room temperature the PXRD profile again remains unchanged indicating a third monotropic phase. Although **3ε** appears stable on cooling to room temperature, attempts to grow crystals of **3ε** by vacuum sublimation across a range of temperatures have so far afforded only **3α** and **3β**. Our attempts to elucidate the structure of **3ε** from the PXRD profile have so far been hampered by the broadness of the diffraction pattern which has precluded reliable indexing. The stability of **3ε** with respect to both **3α** and **3β** suggests that **3ε** is not a simple displacive polymorph (related to either **3α** or **3β** by small molecular or conformational displacements) and likely has a structure significantly different to either of the characterized phases, **3α** and **3β**.

Additional VT-PXRD studies commencing with a pristine sample of **3β** confirmed **3β** was stable to 145 °C with no significant change in the powder pattern (Figure S18) and replicated the transition to **3ε** on heating above 160 °C. Thus both processes, **3α → 3β** and **3β → 3ε**, appear irreversible consistent with monotropic polymorphs. Conversion between monotropic polymorphs is typically considered to be

a reconstructive polymorphic transition, requiring substantial internal restructuring and is often characterized by slow transformations. DSC studies on **3α** (heating rate 5 °C·min^{-1}, considerably faster than the VT-PXRD studies) revealed the presence of a broad endothermic process across the temperature range 120 to 180 °C which is associated with the transformations **3α → 3β → 3ε** but likely comprises a component from sublimation at these elevated temperatures (purification of **3** by sublimation occurred at 130 °C). Despite the broadness of this process a distinct step at 120 °C is consistent with the onset of the process **3α → 3β**, in agreement with the observed change in PXRD pattern associated with the **3α → 3β** transition (Figure S15) while the completion of this process at 180 °C coincides with the **3β → 3ε** transition. DSC studies on pure **3β** at 5 °C/min proved much cleaner with an endothermic transition from **3β** to **3ε** evident in the range 150 – 160 K (ΔH = +17 kJ·mol^{-1}) (Figure S15). The endothermic nature of both processes (**3α → 3β** and **3β → 3ε**) are consistent with entropically driven transitions where the decrease in lattice enthalpy is offset by increases in entropy. In this context the density rule[54] is a well-known, albeit phenomenological approach, for estimating polymorph stability and assumes that the most efficient packing (highest density) reflects the largest enthalpic stability. In the current case **3α** (1.507 g.cm^{-3}) is denser than **3β** (1.407 g.cm^{-3}) in agreement with these observations.

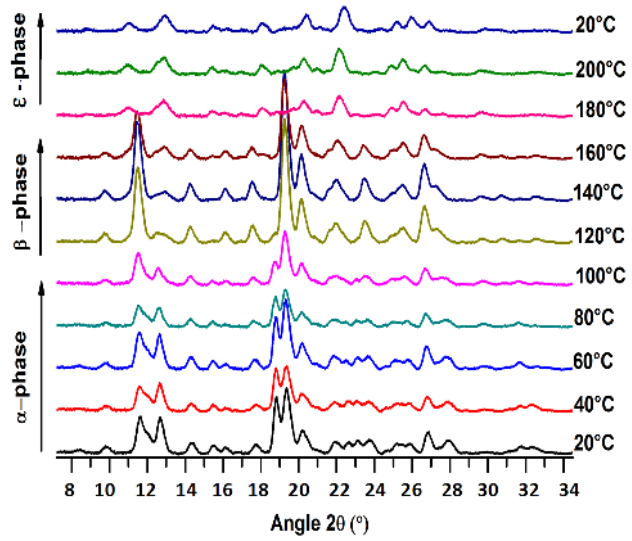

Figure 5: Variable temperature PXRD profiles for a sample of **3α** heated from 20 °C to 200 °C.

Enantiotropic polymorphism: The transformation 3β ↔ 3γ ↔ 3δ: While the transformation from **3α** to **3β** is associated with distinct structural changes (*face-to-face* π–π stacking of anthracenyl groups in **3α** to *edge-to-face* π–π interactions in **3β**), the reversible structural transitions from **3β ↔ 3γ ↔ 3δ** upon cooling are significantly more subtle and diagnostic of displacive polymorphic transitions in which the polymorphs are related by small atomic/molecular displacements. A comparison of the simulated powder patterns for **3β**, **3γ** and **3δ** obtained from single crystal structure determinations indicates they have very similar diffraction profiles despite the changes in the crystal system (orthorhombic **3β** and monoclinic **3γ** and **3δ**) and we resorted to single crystal VT-XRD studies to elucidate the reversibility of the different transitions on heating and cooling (Table S3). A single crystal of **3β** was selected, cooled to 143 K and a series of full data sets and unit cell measurements were collected on warming from 143 – 360 K and then on cooling from 360 K to 143 K. On cooling, **3β** converts to **3γ** below 300 K and then to **3δ** below 165 K. A plot of the temperature dependence of the unit cell parameters (*a*, *b*, c and β) on warming from 143 to 360 K is presented in Figure 6. The transition **3γ ↔ 3β** reflects a switching of *a* and *b* axes and an approximate tripling of the crystallographic *c*-axis. The temperature dependence of the crystallographic cell parameter β is particularly diagnostic of the transitions occurring.

These structural changes are predominantly associated with subtle changes in the periodicity of the intermolecular contacts and each polymorph has a limited window of stability (300 – 433 K for **3β**; 165 – 300 K for **3γ** and < 165 K

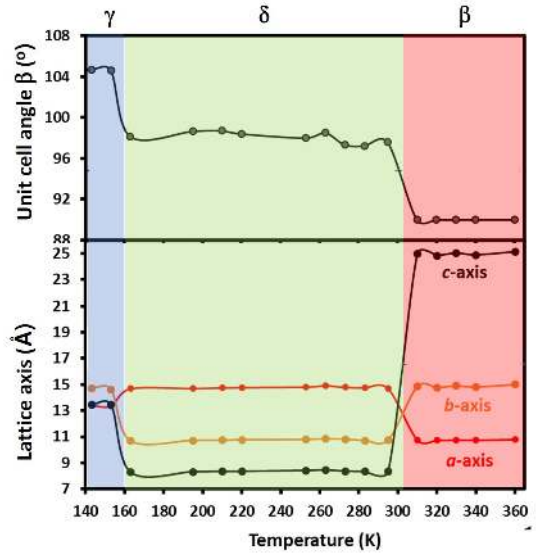

Figure 6: Temperature dependence of the lattice parameters associated with the **3γ ↔ 3δ ↔ 3β** transformations.

for **3δ**). Notably **3β** has Z′ = 3 and three different SN-IV contacts between DTDA radicals whereas **3γ** has Z′ = 1 and forms a regular chain. The low temperature phase **3δ** has Z′ = 2 and exhibits an alternating set of SN-IV contacts. These subtle variations in the nature of the S···N contacts are directly relevant to the analysis of the magnetic response of the **3β ↔3γ ↔ 3δ** system (*vide infra*).

Heat capacity measurements revealed the existence of a transition at 165 K characteristic of the **3γ ↔ 3δ** phase transition (Figure S16) and this transition was also manifested in the temperature dependence of the magnetic susceptibility described below.

Magnetism: Dc magnetic studies on **3α** and **3β/3γ/3δ** were measured on a Quantum Design SQUID magnetometer. Data for **3α** (23 mg) were measured from 5 to 300 K with the sample sealed in a gelatin capsule with an applied field of 1000 Oe. The sample of **3β** (38 mg) was also mounted in a sealed gelatin capsule and measured from 1.8 to 390 K in

both heating and cooling modes with an applied field of 1000 and 10000 Oe.

The temperature dependence of the magnetic susceptibility χ and $1/\chi$ of pristine sample of **3α** are presented in Figure S21. A fit of the data to Curie-Weiss behaviour afforded C = 0.380 cm^3·K·mol^{-1} consistent with S = ½ and g ~ 2.0 (0.375 cm^3·K·mol^{-1}). The Weiss constant (θ = -3.8 K) is indicative of weak antiferromagnetic interactions. At room temperature the χ_mT value is close to the expected value for an uncorrelated S = ½ spin system (0.375 cm^3·K·mol^{-1}). Upon cooling χT decreases slowly, consistent with weak intermolecular antiferromagnetic coupling between S = ½ DTDA radicals. The χT value decreases markedly below 50 K to reach a minimum of 0.277 cm^3·K·mol^{-1} at 5 K. Since the spin density is localized on the heterocyclic ring, the magnetic communication in DTDA radicals often arises through close intermolecular S···S and/or S···N contacts between heterocycles.[51] Based on the intermolecular interactions (Figure 3b), the magnetism of **3α** was modelled as a one-dimensional antiferromagnetic Heisenberg chain with the spin Hamiltonian:

$$\hat{H} = -J \sum_{i=1}^{n} \hat{S}_i \, \hat{S}_{i+1} \qquad \text{Eq. 1}$$

using the Bonner-Fisher equation.[55] Fixing the g value to 2.01 (based on EPR studies) a single parameter fit gave J/k = -5.1 K (Figure 7).

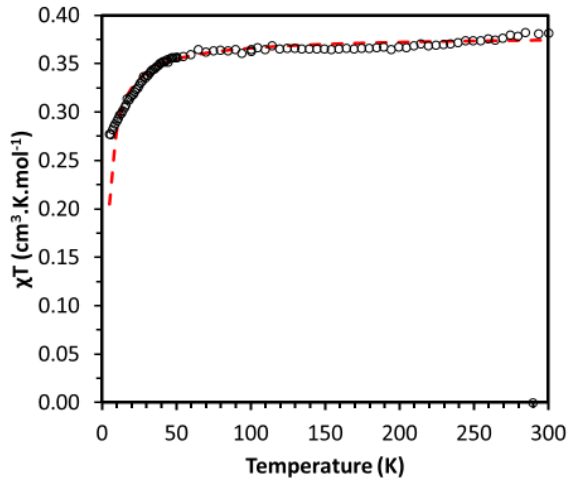

Figure 7: Temperature dependence of χ_mT for **3α**. The red line corresponds to a fit to the Bonner-Fisher model for a uniform 1D magnetic chain (g = 2.01, J/k = -5.1 K).

The magnetic response of **3β** is inherently more complex due to the transformations **3β** ↔ **3γ** ↔ **3δ**. In all cases the SN-IV contacts likely propagate magnetic exchange (*vide infra*). In this context the Hamiltonians for **3β**, **3γ** and **3δ** are respectively Eq. 2, Eq. 1 and Eq.3:

$$\hat{H} = \sum_{i=0}^{n}(-2J\hat{S}_{3i}\hat{S}_{3i+1} - 2J'\hat{S}_{3i+1}\hat{S}_{3i+2} - 2J''\hat{S}_{3i+2}\hat{S}_{3i+3}) \qquad \text{Eq. 2}$$

$$\hat{H} = \sum_{i=0}^{n}(-2J\hat{S}_{2i}\hat{S}_{2i+1} - 2J'\hat{S}_{2i+1}\hat{S}_{2i+2}) \qquad \text{Eq. 3}$$

Standard solutions for Eq. 1 and 3 (Heisenberg linear and alternating chain models) are well known. [53] Conversely a solution to Eq.2 has not been established to our knowledge.

The temperature dependence of χ and χT for a pristine sample of **3β** is presented in Figure 8. The value of χT at 390 K is 0.283 emu·K·mol^{-1} and decreases steadily down to 180 K. Below 180 K there is a small step in the value of χT which is more pronounced in the temperature dependence of χ. which exhibits a small thermal hysteresis window between 150 and 180 K (Figure 8) and coincides with the phase transition **3γ** ↔ **3δ**. Hysteretic phase transitions between diamagnetic π*–π* pancake dimers and paramagnetic monomers is well established in 1,3,2-dithiazolyl radical chemistry[56] but has rarely been observed in DTDA chemistry. Preuss recently reported a hysteretic phase transition in a benzimidazolyl-functionalized DTDA radical associated with breakdown of the π*–π* dimer[57] and stepped temperature dependence of the susceptibility similarly associated with breakdown of DTDA pancake dimers in La(hfac)$_3$(pyDTDA)$_2$ complexes.[58] Awaga and co-workers examined stepwise breakdown of pancake dimers in biphenyl-functionalized bis(DTDA) radicals[59] and other studies have revealed structural transitions in *p*-EtOC$_6$F$_4$CNSSN leading to step changes in magnetic response.[60] In all these previous reports, the magnetic response is linked to the abrupt or progressive breakdown in the long-distance bond-

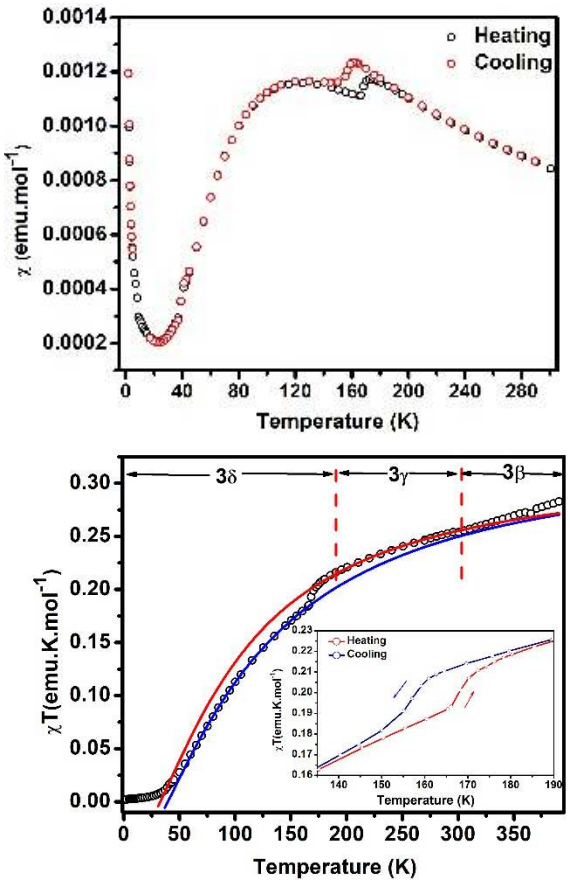

Figure 8: (top) Temperature dependence of magnetic susceptibility for **3β**/**3γ**/**3δ** in heating and cooling modes highlighting the thermal hysteresis associated with the **3γ** ↔ **3δ** transition; (bottom) Temperature dependence of χT for **3β**/**3γ**/**3δ**. Experimental data (circles); red line is the fit to the regular Heisenberg antiferromagnetic chain (J/k = -111 K) and the blue line is the fit to the alternating Heisenberg AF chain (J/k = -158 K, α = 0.78). (Inset) Thermal hysteresis on heating and cooling cycles associated with interconversion between **3γ** and **3δ**.

ing interactions between DTDA radicals. In the current system the hysteresis is associated with a unique paramagnetic-paramagnetic phase transition where the step in χT is associated with a change in the strength of the magnetic exchange coupling. In the absence of an appropriate magnetic model for the high temperature range (300 – 390 K) associated with **3β**, we merely note the (i) decrease in χT upon cooling indicative of dominant antiferromagnetic interactions in this regime and (ii) the value of χT is slightly higher than that computed for **3γ** in this region suggesting slightly weaker exchange couplings in **3β** than **3γ**.

A fit of the magnetic data for **3γ** (180 – 300 K) to Curie-Weiss behaviour affords a Curie Constant C = 0.372 $cm^3 \cdot K \cdot mol^{-1}$ expected for an S = ½ paramagnet and a Weiss constant θ = –138 K consistent with the existence of strong antiferromagnetic interactions (Figure S24). Structural studies in this range suggest a regular Heisenberg chain model should be appropriate (Eq. 1) and a good fit to the experimental data to the Bonner-Fisher model[55] was observed with J/k = -111 K. Below 180 K, **3γ** transforms to **3δ** and the χ *vs* T plot display a broad maximum centered at 125 K indicative of the existence of short-range order (SRO) in **3δ**. The χT *vs* T data for **3δ** were well reproduced using the alternating chain model[55] (Eq. 3) with J/k = -158 K and J'/k = -123 K (J/k = -158 K and the alternation parameter α = 0.78) but fails to reproduce the low temperature data (T < 50 K). This is largely associated with the model which is known to fail at low temperature (T < $J/4k$ ~ 40 K). The value of χT plateaus near 0 $cm^3.K.mol^{-1}$ below *ca.* 40 K consistent with a gapped state with an S = 0 ground configuration. The upturn in χ below 20 K can be attributed to a small fraction of S = ½ paramagnetic defects.

Discussion

The propensity for DTDA radicals to form polymorphs clearly reflects an energy landscape where multiple packing arrangements exist with small energetic differences. While vacuum sublimation removes many of the variables associated with classical solvent recrystallization approaches, there are still several variables which can be tuned and polymorphism arising from sublimation has been discussed by Bernstein *et al*.[54] The polymorphic outcome of crystal growth from sublimation depends on the behaviour of the solid/vapor boundary for each polymorph on the p/T diagram. At a fixed temperature the two polymorphs generally have different vapor pressures and one phase can be isolated, although examples of concomitant DTDA radicals have been identified.[39,61] There have also been cases of so-called "disappearing polymorphs"[62] in DTDA chemistry, although recent work has established that careful choice of sublimation conditions can reveal these elusive less stable polymorphs.[34]

Since **3α** was collected at low temperature, it is considered to be the more enthalpically favourable polymorph whereas **3β** (isolated at elevated temperatures) is considered the more entropically favourable polymorph. The endothermic transformation **3α** → **3β** upon heating confirms that **3β** is entropically more stable than **3α**. The emergence of **3ε** at higher temperatures gives rise to a third monotropic polymorph which are related via reconstructive phase transitions. A comparison of the structures of **3α** and **3β** reveal similar SN-IV interactions but the anthracene functionalities have to undergo substantial structural rearrangements from *face-to-face* to *edge-to-face* π–π interactions, consistent with such a reconstructive process.

In addition to the three monotropic phases described above, **3β** is enantiotropic, exhibiting reversible single-crystal-to-single-crystal phase transitions forming phases **3γ** and **3δ** upon cooling. Here the close similarity in structures (*edge-to-face* π–π interactions coupled with SN-IV contacts) supports the reversible nature of these displacive polymorphic transformations. Indeed it has been noted previously in dithiazolyl (DTA) radical chemistry that the reversible nature of such transformations requires only small atomic displacements.[56,63] Such reversible phase transitions between different polymorphs in DTDA chemistry are extremely rare.[57,59,60,64] The observation of two single-crystal-to-single-crystal transitions between paramagnetic phases associated with **3β** ↔**3γ** ↔ **3δ** is almost unprecedented in DTDA chemistry. The successive breakdown in pancake bonding interactions in Preuss' $Ln(hfac)_3(boaDTDA)_2$ complex, perhaps provides the closest comparison (also two transitions) but a much more pronounced change in magnetic response since the latter is based around cleavage of the enthalpically favorable π*–π* pancake bond, switching from an S = 0 state to two S = ½ spins.[58]

In the current case the lattices of **3β**, **3γ** and **3δ** are similar and comprise a two-dimensional net of SN-IV contacts and edge-to-face π–π contacts (Figure 9). The phase transitions appear to arise from the inherently cooperative nature of this framework in which SN-IV contacts, propagating in one dimension, are cross-braced by C-H···π contacts.

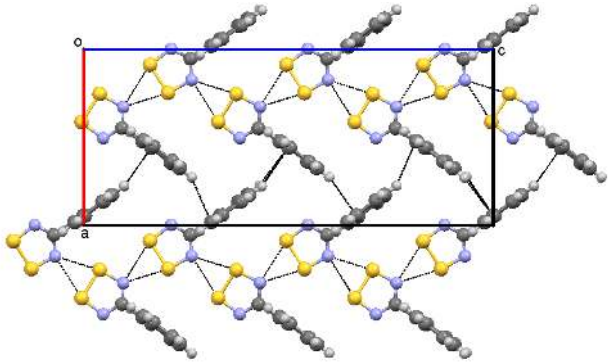

Figure 9: Two-dimensional supramolecular sheet structure common to **3β** (illustrated), **3γ** and **3δ** linked *via* S···N and C-H···π interactions.

In order to review the stepwise processes for the **3δ** ↔**3γ** ↔ **3β** transformations we have focused on three geometric parameters; (i) the intramolecular torsion angle between DTDA and anthracenyl planes, (ii) the intermolecular SN-IV contact common to all polymorphs and (iii) the geometry of the intermolecular edge-to-face anthracenyl contact reflected in the variation in C-H···π distances, the C-H···π angles and the angles formed between the anthracenyl planes. These are presented in Figure 10. Although all three phases

exhibit similar gross packing features, they are discriminated by subtle differences in molecular packing. These are typical of enantiomorphs where the structures are related by small displacive movements of the molecules. It is immediately apparent that the S···N contacts are almost invariant across the temperature range studied, consistent with this being a structure-directing interaction (Figure 10). The transformation from **3δ** to **3γ** on warming is heralded by a marked change in the C-H···π interaction. In **3γ** all the molecules form a C-H···$\pi_{centroid}$ interaction whereas in **3δ** half the molecules forming a C-H···π rather than C-H···$\pi_{centroid}$ interaction. The transformation between these two polymorphs is then related to a small lateral slippage of half the molecules so that the C-H bonds interact with the ring centroid of the π-system rather than a C=C bond. This transition is also associated with a small increase in the angle between anthracenyl planes towards 90° for this edge-to-face interaction. The transformation from **3γ** to **3β** on warming is reflected in an increase in the C-H···π angle, moving closer to a linear interaction. Across the entire temperature range there is a steady increase in the average intramolecular torsion angle between DTDA and anthracenyl rings from 72 to 84°. This corresponds to small displacements either side of the gas-phase optimized geometry (77°, Figure S11), suggesting little inherent strain in the molecule itself. However there is a step in the temperature dependence of this torsion angle associated with the **3γ → 3β** transition. With the invariant nature of the SN-IV contact across this temperature

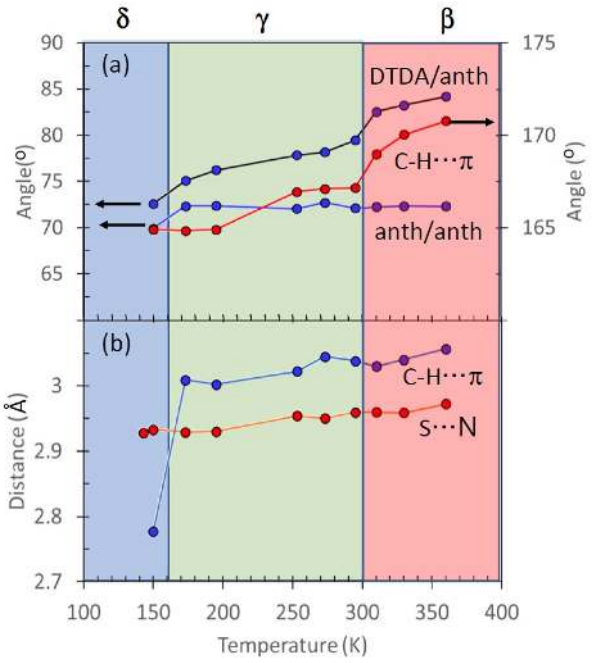

Figure 10: Temperature dependence of (a) selected angles and (b) selected intermolecular contacts for **3β**, **3γ** and **3δ**. The angles correspond to the average torsion angle between (i) DTDA and anthracenyl planes, (ii) the average C-H···$\pi_{centroid}$ angle, (iii) the average angle between anthracenyl planes forming C-H···π contacts. Distances refer to average S···N and C-H···π contacts.

range the phase transitions appear driven by the need to optimize the edge-to-face π–π contacts within the accompanying thermal lattice expansion.

It is noteworthy that the cleavage (and reformation) of energetically significant structure-directing intermolecular contacts appears necessary for the observation of hysteresis. This phenomenon has been well-studied in π-stacked 1,3,2-DTA radicals (Scheme 1).[63] Elegant computational work by Novoa has shown that vibrational entropy plays a key role in driving such transformations. In the current case the hysteresis associated with the **3δ/3γ** transformation likely arises from the necessary lateral slippage on moving from C-H···π to C-H···$\pi_{centroid}$. The inherent increase in entropy on warming within the enantiomorphic **3β/3γ/3δ** system indicates that the enthalpic stabilities are **3δ** > **3γ** > **3β** and this is consistent with expectations based on the density rule and that these transformations are entropy driven.

The fluorescent properties of **3**/**3**$^+$ in solution reveals similar behavior to **1**/**1**$^+$ and **2**/**2**$^+$ systems.[26,27] Previous studies on **2** and **2**$^+$ revealed that the incomplete quenching of fluorescence emission is the result of the inefficiency of the electron exchange (EC) and/or electron transfer (ET) processes between the radical and pyrene moiety in the excited state.[27] Recently the effect of the dihedral angle on a range of substituted-anthracene derivatives on the internal charge transfer between an electron donor or acceptor moiety and anthracene moiety has been investigated.[65] Planar π-conjugated substituted-anthracenes led not only to a red-shift of the absorption bands and an increase in the molar absorption coefficient, but also yield a substantial increase in the fluorescence quantum yield over non-planar variants. In this context the large twist angle between DTDA and anthracenyl rings associated with **3** is consistent with a similar charge transfer quenching process. Notably the twist angle for **3** is much larger than **1** and **2** and is reflected in a much lower quantum yield than either **1** or **2**.

Conclusions

The near orthogonal orientations of the PAH and DTDA rings – driven by substitution at the 9-position of the anthracenyl group – appears to suppress dimerization *via* long-distance multi-centre pancake bonding in **3**, a common feature of DTDA chemistry. This contrasts with the more planar **1** and **2** in which the substitution pattern favors *face-to-face* π - π interactions forming diamagnetic pancake dimers. This design strategy offers access to a range of multi-functional materials combining fluorophores and paramagnetic centres. While compounds such as **1** and **2** display photoluminescence, electroluminescence and a photocurrent in the solid state, compound **3** provides the first example of a multi-functional DTDA radical in which the paramagnetic properties of the radical are combined with the emissive properties of the poly-aromatic hydrocarbons (PAHs) in the solid state. In addition, radical **3** exhibits an extremely rich phase behavior, combining both monotropic (**3α → 3β → 3ε**) and enantiotropic single-crystal-to-single-crystal (**3β ↔ 3γ ↔ 3δ**) phase transitions, with thermal hysteresis evident for the **3γ ↔ 3δ** transition. Detailed structure analysis across this enantiomorphic set provides evidence for

the dominance of the SN-IV contact as a structure-directing motif with the series of phase changes upon warming, associated with subtle changes in the edge-to-face interactions between anthracenyl groups. While the large torsion angle between DTDA and 9'-anthracenyl group suppresses dimer formation, it also seems effective at reducing fluorescence quantum yields and a balance between these two effects is required to generate paramagnetic DTDA radicals with good quantum efficiencies.

Experimental

A. Material and Methods

9-bromoanthracene (**4**), *n*-butyllithium, bis(trimethylsilyl) carbodiimide, silver powder and sulfur monochloride were used as supplied (Sigma-Aldrich). Sulfur dichloride (SCl_2) was prepared from sulfur monochloride (S_2Cl_2) according to the literature method.[66] Dry solvents; tetrahydrofuran (THF), diethylether (Et_2O), and acetonitrile (MeCN) (Sigma-Aldrich) were used without any further purification. Gallium trichloride (Strem Chemicals) was used as received. EPR spectra were recorded on a Bruker EMXplus EPR spectrometer at room temperature. All UV-visible spectroscopic studies were conducted on a G103A Agilent spectrophotometer. Fluorescence spectroscopy was carried out on a Varian fluorescence spectrometer. Cyclic voltammetry measurements were run using a CH Instruments electrochemical work station model CHI760E. Differential Scanning Calorimetry studies on **3** were performed on a Mettler Toledo DSC 822e with nitrogen (99.99%) used to purge the system at a flow of 60 mL/min. Powder XRD measurements were recorded on a Bruker D8 Discover diffractometer equipped with a Hi-Star area detector and GADDS software package. The tube was operated at 40 kV and 40 mA using Cu-Kα_1 radiation (λ=1.54187 Å) with a beam diameter of 0.5 mm. The temperature was controlled using an Oxford Cryosystems Cryostat (700 Series Cryostream Plus). Time-dependent DFT calculations were carried out on the optimized gas-phase geometry using the unrestricted B3LYP functional and 6-311G*+ triple zeta basis set.

Single crystal X-ray diffraction studies were measured on a Bruker APEX-II diffractometer using Mo-Kα radiation (λ = 0.71079 Å) or Cu-Kα radiation (λ = 1.5407 Å) equipped with an Oxford cryostream variable temperature device. Data were collected using the Bruker APEX-II program,[67] integrated with SAINT[68] and an absorption correction (SADABS)[69] applied, an empirical correction for crystal decay was applied. The structure was solved using direct methods and all atoms refined anisotropically using full matrix least squares on F^2.[70] Structures of **3α, 3β, 3γ** and **3δ** collected in temperature range 143 K–360 K have been deposited with the CCCDC (CCCDC deposition numbers 1874989 – 1874995 and 1894313 – 1894316). Unit cell parameters and information on final residuals are presented in Table 1. Magnetic measurements of **3α** were made on a Quantum Design MPMS SQUID magnetometer in dc mode in applied fields between 0.1 and 1.0 T in the range 5 – 300 K, while magnetic measurement of **3β** were made on a Quantum Design MPMS SQUID magnetometer in dc mode in applied fields between 1 T in the range 1.8 – 390 K. Additional magnetic studies were undertaken on **3β** on heating and cooling cycles.

Preparation of the dithiadiazolylium chloride salt **[3]Cl**

9-Bromoanthracene (3.9 mmol, 1.00 g) was dissolved in diethyl ether (30 ml) and cooled to -78 °C. Butyl lithium (10 M, 4 mmol, 0.40 ml) was added dropwise and the reaction left to stir for 1 h under argon. Bis(trimethylsilyl) carbodiimide (3.39 mmol, 0.88 ml) was added to the mixture and the reaction was left to stir at room temperature for 24 h to afford a pale red solution. SCl_2 (7.82 mmol, 0.50 ml) was added dropwise with vigorous stirring to yield, after complete addition of SCl_2, a yellow/green solid under an orange solution. After filtration, washing with diethyl ether and drying under vavuum, crude [**3**]Cl was isolated as a yellow/green powder contaminated with LiCl. Yield: 1.3 g. Its poor solubility across a variety of solvents precluded full characterization but treatment with $GaCl_3$ afforded the soluble $GaCl_4^-$ salt which was characterized by multinuclear NMR, elemental analysis, UV/vis spectroscopy and mass spectrometry (see C).

B. *Preparation of the dithiadiazolyl radical 3*

Silver powder (0.170 g, 1.58 mmol) was stirred with the solid chloride salt [**3**]Cl (0.50 g, 1.58 mmol) in THF under argon. The reaction was left to stir for 12 h to afford a dark solution. The solid residue was filtered off and the solvent was evaporated *in vacuo* to afford a dark residue, which was purified by vacuum sublimation to afford black crystals of the radical. Yields were unoptimized but provided sufficient sample for compound characterization.

HRMS: $[M+H]^+$ = 282.0.289 (calc. 282.0285), Microanalytical data: Observed (calculated) C = 64.3 (64.0), H = 2.9 (3.2), N = 9.9 (9.6)%. EPR (X-band: dry THF, 298 K): g = 2.010, a_N = 5.10 G. The radical was additionally characterized by single crystal X-ray diffraction, powder X-ray diffraction (for phase purity), SQUID magnetometry. UV/vis absorption and emission spectra were also recorded (see Results and Discussion sections).

3α was selectively obtained by sublimation (130 °C) onto a cold-finger maintained at -15 °C. Yield: 30 mg (7 %),

3β was selectively obtained by sublimation (130 °C) onto a 'cold-finger' maintained in the range 50 to 70 °C. Yield: 15 mg (3 %),

Preparation of [3][GaCl₄]

Gallium chloride (0.138 g, 0.79 mmol) was stirred with as-prepared [**3**]Cl (0.25 g, 0.79 mmol) in THF under an argon atmosphere for 2 h. The solid residue was filtered off and the solvent evaporated *in vacuo* to afford a dark residue. Yield: 320 mg (82 %), MS(EI+): M^+ = 280.9; ^{1}H NMR (500 MHz, $CDCl_3$) δ 8.75 (s, 1H), 8.14 (d, 2H), 8.08 (d, 2H), 7.75 (t, 2H), 7.63 (t, 3H). ^{13}C NMR (126 MHz, $CDCl_3$) δ 167.2, 132.5, 130.5, 129.4, 129.1, 128.3, 126.4, 122.8, 121.5; Microanalytical data: Observed (calculated) C% = 37.4 (36.6), H% =1.6 (1.8), N%= 5.1(5.6).

C. Preparation of thin films for solid-state studies

Solid films of **3** were prepared by drop-casting on a surface of a quartz slides under inert conditions using a highly concentrated solution of **3** in THF. After solvent evaporation, highly air-sensitive solid thin purple films of the radical **3** were formed. The films were protected from moisture by another quartz slide. Thin films of [**3**][$GaCl_4$] and **4** were made in the same fashion. All measurements were made at room temperature.

ASSOCIATED CONTENT

Supporting Information: Crystallographic information for **3α** before and after UV irradiation. A summary of the crystallographic studies of **3β** after UV irradiation; Crystallographic information for the different polymorphs of **3β** at different temperatures are reported in cif format; EPR and electrochemical studies on **3** in solution**;** UV/vis absorption and emission studies on **3** in solution and PMMA matrix; emission studies of **3** in the solid state; The gas phase optimized molecular structure of **3** and $\mathbf{3}^{+}$; information on TD-DFT calculations undertaken on **3**; DSC studies on **3**; Powder X-ray diffraction studies of **3** at variable temperatures; Detail of the magnetic studies of **3α** and **3β**. This material is available free of charge *via* the Internet at **http://pubs.acs.org**

AUTHOR INFORMATION

Corresponding Author

* J.M. Rawson, Dept of Chemistry and Biochemistry, The University of Windsor, 401 Sunset Avenue, Windsor, ON, N9B 3P4, CANADA. E-mail: jmrawson@uwindsor.ca

Present Addresses

† Northwestern University, 2145 Sheridan Road, Evanston, Illinois, USA, 60208.

Author Contributions

All authors have given approval to the final version of the manuscript.

Funding Sources

We would like to thank the Canada Research Chairs Program for financial support (J.M.R.), the University of Windsor for a scholarship (Y.B.). E.G and M.P would like to thank NSERC. A.A and J.C acknowledge support from grant MAT2015-68200-C2-2-P from the Ministerio de Economía y Competividad of Spain and the European Regional Development Fund. Additional support from Diputación General de Aragón (DGA-M4) is also acknowledged.

ABBREVIATIONS

DTDA, dithiadiazolyl; DTA, dithiazolyl; PAH, poly-aromatic hydrocarbon; OFET, organic field-effect transistor; OLED, organic light-emitting diode; EPR, electron paramagnetic resonance; SOMO, single occupied molecular orbital; HOMO, highest occupied molecular orbital; LUMO, lowest unoccupied molecular orbital; TEMPO, 2,2,6,6-Tetramethylpiperidin-1-yl)oxyl; SQUID, superconducting quantum interference design; AF, Antiferromagnetic; SRO, Short Range Order; TTTA, trithiatriazapentalenyl; DFT, density functional theory; hfac, Hexafluoroacetylacetone; pyDTDA, (2′-pyridyl)-1,2,3,5-dithiadiazolyl); TD-DFT, time dependent density functional theory; DPA, diphenyl anthracene; PMMA, Poly(methyl methacrylate).

REFERENCES

1. (a) Chen, M.; Yan, L.; Zhao, Y.; Murtaza, I.; Meng, H.; Huang, W. Anthracene-based semiconductors for organic field-effect transistors. *J. Mater. Chem. C.*, **2018**, 6, 7416 – 7444. (b) Wang, Q.; Jiang, S.; Qian, J.; Song, L.; Zhang, L.; Zhang, Y.; Zhang, Y.; Wang, Y.; Wang, X.; Shi, Y.; Zheng, Y.; Li, Y. Low-voltage, High-performance Organic Field-Effect Transistors Based on 2D Crystalline Molecular Semiconductors. *Sci. Rep.,* **2017**,7, 7830. (c) Nishida, J.; Ando, S.; Yamaguchi, J.; Itaka, K.; Koinuma, H.; Tada, H.; Tokito, S.; Yamashita, Y. High-Performance Organic Field-Effect Transistors Based on π-Extended Tetrathiafulvalene Derivatives. *J. Am. Chem. Soc.*, **2005**, 127, 10142 – 10143.

2. (a) Rajamalli, P.; Senthilkumar, N.; Gandeepan, P.; Huang, P.-Y.; Huang, M.-J.; Ren-Wu, C.-Z.; Yang, C.-Y.; Chiu, M.-J.; Chu, L.-K.; Lin, H.-W.; Cheng, C.-H. A New Molecular Design Based on Thermally Activated Delayed Fluorescence for Highly Efficient Organic Light Emitting Diodes. *J. Am. Chem. Soc.* **2016**, 138, 628 – 634. (b) Lee, J.; Chen, H.-F.; Batagoda, T.; Coburn, C.; Djurovich, P. I.; Thompson, M. E.; Forrest, S. R. Deep blue phosphorescent organic light-emitting diodes with very high brightness and efficiency. *Nat. Mater*. **2016**, *15*, 92 – 98. (c) Wang, S.; Yan, X.; Cheng, Z.; Zhang, H.; Liu, Y.; Wang, Y. Highly Efficient Near-Infrared Delayed Fluorescence Organic Light Emitting Diodes Using a Phenanthrene-Based Charge-Transfer Compound. *Angew. Chem. Int. Ed.* **2015**, *54*, 13068 – 13072. (d) Nakanotani, H.; Higuchi, T.; Furukawa, T.; Masui, K.; Morimoto, K.; Numata, M.; Tanaka, H.; Sagara, Y.; Yasuda T.; Adachi, C. High-efficiency organic light-emitting diodes with fluorescent emitters. *Nature Comm*. **2014**, *5*, 4016. (e) Suzuki, K.; Kubo, S.; Shizu, K.; Fukushima, T.; Wakamiya, A.; Murata, Y.; Adachi, C.; Kaji, H. Triarylboron-Based Fluorescent Organic Light-Emitting Diodes with External Quantum Efficiencies Exceeding 20 %. *Angew. Chem.* **2015**, *127*, 15446 – 15450. (f) Aizawa, N.; Pu, Y.-J.; Watanabe, M.; Chiba, T.; Ideta, K.; Toyota, N.; Igarashi, M.; Suzuri, Y.; Sasabe H.; Kido, J. Solution-processed multilayer small-molecule light-emitting devices with high-efficiency white-light emission. *Nature Comm*. **2014**, *5*, 5756. (g) Lee, S. Y., Yasuda, T., Yang, Y. S., Zhang, Q. and Adachi, C. Luminous butterflies: efficient exciton harvesting by benzophenone derivatives for full-color delayed fluorescence OLEDs. *Angew. Chem. Int. Ed.* **2014**, *53*, 6402 – 6406. (h) Zhu, M.; Yang, C. *Chem. Soc. Rev*. **2013**, *42*, 4963 – 4976. (i) Farinola, G. M.; Ragni, R. Electroluminescent materials for white organic light emitting diodes. *Chem. Soc. Rev.* 2011, *40*, 3467 – 3482. (j) Chercka, D.; Yoo, S-J.; Baumgarten, M.; Kim, J-J.; Müllen, K. Pyrene based materials for exceptionally deep blue OLEDs. *J. Mater. Chem. C* **2014**, ***2***, 9083 – 9086.

3. (a) Zhan, X.; Sun, N.; Wu, Z.; Tu, J.; Yuan, L.; Tang, X.; Xie, Y.; Peng, Q.; Dong, Y.; Li, Q.; Ma, D. ; Li, Z. Polyphenylbenzene as a Platform for Deep-Blue OLEDs: Aggregation Enhanced Emission and High External Quantum Efficiency of 3.98%. *Chem. Mater*. **2015**, 27, 1847 – 1854. (b) Cui, X.; Xiao, C.; Zhang, L.; Li, Y.; Wang, Z. Polycyclic aromatic hydrocarbons with orthogonal tetraimides as n-type semiconductors. *Chem. Commun.* **2016**, 52, 13209 – 13212. (c) Winzenberg, K.N.; Watkins, S.E.; Kemppinen, K.P.; Bown, M. **2010**. *U.S. Patent Application No. 13/254,443*. (d) Lehnherr, D.; Tykwinski, R.R. Conjugated Oligomers and Polymers Based on Anthracene, Tetracene, Pentacene, Naphthodithiophene, and Anthradithiophene Building Blocks. *Aust. J. Chem.* **2011**, *64*, 919 – 929. (e) Li, J.; Terec, A.; Wang, Y.; Joshi, H.; Lu, Y.; Sun, H.; Stuparu, M. C. π-Conjugated Discrete Oligomers Containing Planar and Nonplanar Aromatic Motifs. *J. Am. Chem. Soc.* **2017**, 139, 3089 – 3094.

4. (a) Tuček, J.; Holá, K.; Bourlinos, A. B.; Błoński, P. ; Bakandritsos, A.; Ugolotti, J.; Dubecký, M.; Karlický, F.; Ranc,V.; Čépe, K.; Otyepka, M.; Zbořil, R. Room temperature organic magnets derived from sp^3 functionalized graphene. *Nature*

Commun., **2017**, 8, 14525. (b) Miller, J. S. Organic- and molecule-based magnets. *Mater. Today* **2014**, 16, 224 – 235.
5. Taniguchi, T.; Sugiyama, H. ; Uekusa, H.; Shiro, M.; Asahi, T.; Koshima H. Walking and rolling of crystals induced thermally by phase transition. *Nature Commun.,* **2018***, 9*, 538.
6. Sagara, Y.; Kato, T. Mechanically induced luminescence changes in molecular assemblies. *Nature Chem.,* **2009**, *1*, 605 – 610.
7. (a) Ohshima, S.; Morimoto, M.; Irie, M. Light-driven bending of diarylethene mixed crystals. *Chem. Sci.*, **2015**, 6, 5746 – 5752. (b) Phan, H.; Lekin, K.; Winter, S. M.; Oakley, R. T.; Shatruk, M. Photoinduced Solid State Conversion of a Radical σ-Dimer to a π-Radical Pair. *J. Am. Chem. Soc.* **2013**, 135, 15674 – 15677.
8. Oto, O. Dynamic molecular crystals with switchable physical properties. *Nature Chem*. **2016**,8, 644 – 656.
9. (a) J. A. Green, L. A. Singer and J. H. Parks, J. Chem. Phys., 1973, 58, 2690–2695; (b) M. Laferrie`re, R. E. Galian, V. Maurela and J. C. Scaiano, Chem. Commun., 2006, 257–259; (c) C. Tansakul, E. Lilie, E. D. Walter, F. Rivera, A. Wolcott, J. Z. Zhang, G. L. Millhauser and R. Braslau, J. Phys. Chem. C, 2010, 114, 7793–7805; (d) F. Lin, D. Pei, W. He, Z. Huang, Y. Huang and X. Guo, J. Mater. Chem., 2012, 22, 11801–11807; N. V. Blough and D. J. Simpson, J. Am. Chem. Soc., 1988, 110, 1915–1917; D. Matuschek, S. Eusterwiemann, L. Stegemann, C. Doerenkamp, B. Wibbeling, C. G. Daniliuc, N. L. Doltsinis, C. A. Strassert, H. Eckert and A. Studer, Chem. Sci., 2015, 6, 4712–4716.
10. Peng, Q.; Obolda, A.; Zhang, M.; Li, F. Organic Light-Emitting Diodes Using a Neutral π Radical as Emitter: The Emission from a Doublet, *Angew. Chem. Int. Ed.*, **2015**, 54, 7091 – 7095.
11. Stable Radicals: Fundamentals and Applied Aspects of Odd-Electron Compounds (Ed. Hicks, R.G.), Wiley VCH **2010**.
12. (a) Thomson, R. I.; Pask, C. M.; Lloyd, G. O.; Mito, M.; Rawson, J. M. Pressure-Induced Enhancement of Magnetic-Ordering Temperature in an Organic Radical to 70 K: A Magnetostructural Correlation. *Chem. Eur. J.* **2012**, 18, 8629 – 8633.
13. (a) Mailman, A.; Winter, S. M.; Wong, J. W. L.; Robertson, C. M.; Assoud, A.; Dube, P. A.; Oakley, R.T. Multiple Orbital Effects and Magnetic Ordering in a Neutral Radical. *J. Am. Chem. Soc.*, **2015**, 137, 1044 – 1047. (b) Leitch, A. A.; Brusso, J. L.; Cvrkalj, K.; Reed, R. W.; Robertson, C. M.; Dube, P. A.; Oakley, R. T. Spin-canting in heavy atom heterocyclic radicals. *Chem. Commun.*, **2007**, 3368 – 3370. (c) Winter, S. M.; Oakley, R. T.; Kovalev, A. E.; Hill, S. Spin-orbit effects in heavy-atom organic radical ferromagnets. *Phys. Rev. B*, **2012**, 85, 094430. (d) Yu, X.; Mailman, A.; Lekin, K.; Assoud, A.; Robertson, C. M.; Noll, B. C.; Campana, C. F.; Howard, J. A. K.; Dube, P. A.; Oakley, R. T. Semiquinone-Bridged Bisdithiazolyl Radicals as Neutral Radical Conductors. *J. Am. Chem. Soc.*, **2012**, 134, 2264 – 2275.
14. Iwasaki, A.; Hu, L.; Suizu, R.; Nomura, K.; Yoshikawa, H.; Awaga, K.; Noda, Y.; Kanai, K.; Ouchi, Y.; Seki, K.; Ito, H. Interactive Radical Dimers in Photoconductive Organic Thin Films. *Angew Chem. Int. Ed.* **2009**, 48, 4022 – 4024.
15. (a) Bates, D.; Robertson, G. M.; Leitch,A. A.; Dube, P. A.; Oakley, R. T. Magnetic Bistability in Naphtho-1,3,2-dithiazolyl: Solid State Interconversion of a Thiazyl π-Radical and Its N–N σ-Bonded Dimer. *J. Am. Chem. Soc.*, **2018**, *140*, 3846 – 3849. (b) Lekin, K.; Phan, H.; Winter, S. M.; Wong, J. W. L.; Leitch, A. A.; Laniel, D.; Yong, W.; Secco, R. A.; Tse, J. S.; Desgreniers, S.; Dube, P. A.; Shatruk, M.; Oakley, R. T. Heat, Pressure and Light-Induced Interconversion of Bisdithiazolyl Radicals and Dimers. *J. Am. Chem. Soc.,* **2018***, 136*, 8050 – 8062. (c) Wong, J. W. L.; Mailman, A.; Lekin, K.; Winter, S. M.; Yong, W.; Zhao, J.; Garimella, S. V.; Tse, J. S.; Secco, R. A.; Desgreniers, S.; Ohishi, Y.; Borondics, F.; Oakley, R. T. Pressure Induced Phase Transitions and Metallization of a Neutral Radical Conductor. *J. Am. Chem. Soc*., **2014**, 136, 1070 – 1081. (d) Tian, D.; Winter, S. M.; Mailman, A.; Wong, J. W. L.; Yong, W.; Yamaguchi, H.; Jia, Y.; Tse, J. S.; Desgreniers, S.; Secco, R. A.; Julian, S. R.; Jin, C.; Mito, M.; Ohishi, Y.; Oakley, R. T. The Metallic State in Neutral Radical Conductors: Dimensionality, Pressure and Multiple Orbital Effects. *J. Am. Chem. Soc.,* **2015***, 137*, 14136 – 14148.
16. Mulliken, R.S.; Person, W.B. Molecular Complexes, Wiley-Interscience, **1969**.
17. (a) Beneberu, H. Z.; Tian, Y.-H.; Kertesz, M. Bonds or not bonds? Pancake bonding in 1,2,3,5-dithiadiazolyl and 1,2,3,5-diselenadiazolyl radical dimers and their derivatives. *Phys.Chem.Chem.Phys.*, **2012**, 14, 10713 – 10725. (b) Preuss, K. E. Pancake bonds: π-Stacked dimers of organic and light-atom radicals. *Polyhedron*, **2014**, 79, 1 – 15.
18. Banister, A.J.; Smith, N.R.M.; Hey, R.G. The preparation of some 4-phenyl-1,2,3,5-dithiadiazolium salts and a dimeric 4-phenyl-1 ,2,3,5-dithiazole, $(PhCN_2S)_2$. *J. Chem. Soc., Perkin Trans. I*, **1983**, 1181 – 1186.
19. see for example: Del Sesto, R.E.; Miller, J. S.; Lafuente, P, Novoa, J.J. Exceptionally Long (≥2.9 Å) CC Bonding Interactions in π-$[TCNE]_2^{2-}$ Dimers: Two-Electron Four-Center Cation-Mediated CC Bonding Interactions Involving π* Electrons, *Chem. Eur. J*., **2002**, 8, 4894 – 4908; Miller, J.S. Four-Center Carbon−Carbon Bonding, *Accts. Chem. Res*., **2007**, *40*, 189 – 196.
20. (a) Phan, H.; Lekin, K.; Winter, S. M.; Oakley, R. T.; Shatruk, M. Photoinduced Solid State Conversion of a Radical σ-Dimer to a π-Radical Pair. *J. Am. Chem. Soc.*, **2013**, 135, 15674 – 15677.
21. Cordes, A.W.; Haddon, R. C.; Oakley, R. T. Molecular conductors from neutral heterocyclic π-radicals. *Adv Mater.*, **1994**, 6, 798 – 802.
22. (a) Preuss, K. E. Metal-radical coordination complexes of thiazyl and selenazyl ligands. *Coord. Chem. Rev.*, **2015**, 289 – 290 , 49 – 61. (b) Fatila, E. M.; Clérac, R.; Rouzières, M.; Soldatov, D. V.; Jennings, M.; Preuss, K. E. Ferromagnetic superexchange in a 1D –[LaIII–radical]– coordination polymer. *Chem. Commun*., **2013**, 49, 6271 – 6273; (c) Haynes, D. A., van Laeren, L. J., Munro, O. Q. Cobalt Porphyrin–Thiazyl Radical Coordination Polymers: Toward Metal–Organic Electronics. *J. Am. Chem. Soc.*, **2017**, 139, 14620 – 14637.
23. (a) Boeré, R. T.; Moock, K. H.; Parvez, M. Electrochemical evidence for the existence of three stable oxidation states for heterocycles of the type $XC_6H_4CN_2E_2$ (E = S, Se). X-ray crystal structure of the dimer with X = Cl, E = S. *Z. Anorg. Allg. Chem*. **1994**, 620, 1589 – 1598. (b) Aherne, C. M.; Banister, A. J.; Gorrell, I. B.; Hansford, M. I.; Hauptman, Z. V.; Luke, A. W.; Rawson, J. M. Electrochemical studies of some dithiadiazolylium cations; evidence for the dithiadiazolide anion, $[PhCNSSN]^-$. *Dalton Trans.*, **1993**, 967 – 972. (c) Aherne, C. M.; Banister, A. J.; Hibbert, T. G.; Luke, A. W.; Rawson, J.M. The preparation of, and electrochemical studies on, some substituted aryl dithiadiazolylium salts and dithiadiazolyl radicals. *Polyhedron* **1997**, 16, 4239 – 4245.
24. Luzon, J.; Campo, J.; Palacio, F.; McIntyre, G. J.; Rawson, J. M.; Less, R.J.; Pask, C. M.; Alberola, A.; Farley, R. D.; Murphy, D. M., Goeta A. E. Spin density studies on *p*-$O_2NC_6F_4CNSSN$: A heavy *p*-block organic ferromagnet. *Phys. Rev. B* **2010**, 81, 144429.
25. Haynes, D. A. Crystal engineering with dithiadiazolyl radicals. *CrystEngComm.*, **2011**,13, 4793 – 4805.
26. Beldjoudi, Y.; Osorio.-Román, I.; Nascimento, M. A.; Rawson, J. M. A fluorescent dithiadiazolyl radical: structure and optical properties of phenanthrenyl dithiadiazolyl in solution and polymer composites. *J. Mater. Chem. C* , **2017**, **5**, 2794 – 2799.
27. Beldjoudi, Y.; Nascimento, M. A.; Cho, Y. J.; Yu, H.; Aziz, H.; Tonouchi, D.; Eguchi, K.; Matsushita, M. M.; Awaga, K.; Osorio-Roman, I.; Constantinides, C. P.; Rawson, J. M. Multifunctional Dithiadiazolyl Radicals: Fluorescence, Electroluminescence, and Photoconducting Behavior in Pyren-1′-yl-dithiadiazolyl. *J. Am. Chem. Soc.*, **2018**, 140, 6260–6270.
28. Alberola, A.; Clarke, C.S.; Haynes, D.A.; Pascu, S.I.; Rawson, J.M. Crystal structures and magnetic properties of a sterically encumbered dithiadiazolyl radical, 2,4,6-$(F_3C)_3C_6H_2CNSSN$, *Chem.Commun.*, **2005**, 4726 – 4728.
29. Alberola, A.; Less, R. J.; Pask, C.M.; Rawson, J. M.; Palacio, F.; Oliete, P.; Paulson, C.; Yamaguchi, A.; Farley, R. D.; Murphy, D. M. A thiazyl-based organic ferromagnet. *Angew. Chem. Int. Ed.* **2003**, 42, 4782 – 4785.
30. Banister, A. J.; Bricklebank, N.; Lavender, I.; Rawson, J.M.; Gregory, C.I., Tanner, B. K.; Clegg W.; Elsegood, M. R.J.; Palacio, F. Spontaneous Magnetization in a Sulfur–Nitrogen Radical at 36 K. *Angew Chem. Int. Ed. Engl.* **1996**, 35, 2533 – 2535.
31. (a) Alberola, A.; Less, R. J.; Palacio, F.; Pask, C.M.; Rawson, J. M. Synthesis and Magnetic Properties of the Novel Dithiadiazolyl Rad-

ical, *p*-$NCC_6F_4C_6F_4CNSSN$. *Molecules*, **2004**, 9, 771 – 781. (b) Antorrena, G.; Davies, J. E.; Hartley, M.; Palacio, F.; Rawson, J. M.; Smith, J. N. B.; Steiner, A. A novel paramagnetic dithiadiazolyl radical: Crystal structure and magnetic properties of *p*-BrC_6F_4CNSSN. *Chem. Commun.*, **1999**, 1393 – 1394. (c) Banister, A. J.; Bricklebank, N.; Clegg, W.; Elsegood, M. R. J.; Gregory, C. I.; Lavender, I.; Rawson, J. M.; Tanner, B. K. The first solid state paramagnetic 1,2,3,5-dithiadiazolyl radical; X-ray crystal structure of [*p*-NCC_6F_4CNSSN] *J. Chem. Soc., Chem. Commun.*, **1995**, 679 – 680.

32. A search of the CSD (2017 release) revealed 15 structures containing a CN_2 fragment attached to a 9'-anthracenyl backbone. Two structures (PEXGII and ENIYOP) were omitted due to disorder or significant structural distortions in the refinement. The average of the remaining torsion angles in this set was 52.3°.

33. Nascimento, M.A.; Rawson, J.M. 1,2,3,5-Dithiadiazolyl Radicals, *Encycl. Inorg. Bioinorg. Chem.*, J. Wiley, **2019**, accepted manuscript (manuscript eibc2640.R1).

34. Beldjoudi, Y.; Arauzo, A.; Palacio, F.; Pilkington, M.; Rawson, J. M. Studies on a "Disappearing Polymorph": Thermal and Magnetic Characterization of α-*p*-NCC_6F_4CNSSN. *J. Am. Chem. Soc.,* **2016**, 138*,* 16779 – 16786.

35. Cruz-Cabeza, A.J.; Bernstein, J. Conformational Polymorphism, *Chem. Rev*. **2014**, 114, 2170 – 2191.

36. Allen, C.; Haynes, D. A.; Pask, C. M.; Rawson, J. M. Co-crystallisation of thiazyl radicals: preparation and crystal structure of [PhCNSSN][C_6F_5CNSSN] *CrystEngComm.* **2009**, 11, 2048 – 2050.

37. (a) Alberola, A.; Carter, E.; Constantinides, C.P.; Eisler, D.J.; Murphy, D. M.; Rawson, J. M. Crystal structures, EPR and magnetic properties of 2-$ClC_6H_4CNSSN^{\cdot}$ and 2,5-$Cl_2C_6H_3CNSSN$. *Chem. Commun.,* **2011**, *47*, 2532 – 2534. (b) Robinson, S. W.; Haynes, D. A.; Rawson, J. M. Co-crystal formation with 1,2,3,5-dithiadiazolyl radicals. *CrystEngComm.* **2013**, *15*, 10205 – 10211.

38. (a) Clarke, C.S.; Haynes, D.A.; Smith, J.N.B.; Batsanov, A.S.; Howard, J.A.K.; Pascu, S.I.; Rawson, J.M. The effect of fluorinated aryl substituents on the crystal structures of 1,2,3,5-dithiadiazolyl radicals, *CrystEngComm.*, **2010**, *12*, 172 - 185; (b) Fatila, E.M.; Jennings, M.C.; Goodreid, J.; Preuss K.E., A third polymorph of 4-(2,6-difluorophenyl)-1,2,3,5-dithiadiazolyl, *Acta. Crystallogr*, **2010**, C66, o260-o264.

39. (a) Bond, A. D.; Haynes, D. A.; Pask, C. M.; Rawson, J. M. Concomitant polymorphs: structural studies on the trimorphic dithiadiazolyl radical, ClCNSSN. *J. Chem. Soc., Dalton Trans.*, **2002**, 2522 – 2531; (b) Clarke, C.S.; Pascu, S.I.; Rawson J.M. Further studies on the polymorphic dithiadiazolyl radical, ClCNSSN, *Cryst.Eng.Comm.***2004**, *6*, 79 – 82; (c) Knapp, C.; Lork, E.; Gupta, K.; Mews, R. Structure Investigations on 4-Halo-1,2,3,5-dithiadiazolyl Radicals XCNSSN• (X = F, Cl, Br): The Shortest Intradimer S···S Distance in Dithiadiazolyl Dimers, *Z. Anorg. Allg. Chem.*, **2005**, 631, 1640 -1644.

40. Britten, J.; Hearns, N. G. R.; Preuss, K. E.; Richardson, J. F.; Bin-Salamon, S. Mn(II) and Cu(II) Complexes of a Dithiadiazolyl Radical Ligand: Monomer/Dimer Equilibria in Solution. *Inorg. Chem.*, **2007**, *46*, 3934-3945.

41. Chandros, E. A.; Sonntag, F. I. Chemiluminescent Electron-Transfer Reactions of Radical Anions. *J. Am. Chem. Soc.,* **1966**, 88, 1089 – 1096.

42. Zouev, I.; Cao, D.-K.; Sreevidya, T. V.; Telzhensky, M.; Botoshansky, M.; Kaftory, M. Photodimerization of anthracene derivatives in their neat solid state and in solid molecular compounds. *CrystEngComm*, **2011**, 13, 4376 – 4381

43. Nakatsuji, S.; Ojima, T.; Akutsu, H.; Yamada, J. Anthracene Derivatives and the Corresponding Dimers with TEMPO Radicals. *J. Org. Chem.*, **2002**, 67, 916–921.

44. Ramamurthy, V.; Venkatesan K. Photochemical reactions of organic crystals, *Chem. Rev.*, **1987**, *87*, 433 – 481.

45. (*a*) Tang, C. W.; Vanslyke, S.A. Organic electroluminescent diodes. *Appl. Phys. Lett.*, **1987**, 51, 913 – 915. (*b*) Huang, J.; Wang, X.; deMello, A. J.; deMello, J. C.; Bradley, D. D. C. Efficient flexible polymer light emitting diodes with conducting polymer anodes. *J. Mater. Chem.*, **2007**, 17, 3551 – 3554. (*c*) D'Andrade, B. W.; Forrest, S. R. White Organic Light-Emitting Devices for Solid-State Lighting. *Adv. Mater.*, **2004**, 16, 1585 – 1595. (*d*) Uoyama, H.; Goushi, K.; Shizu, K.; Nomura, H.; Adachi, C. Highly efficient organic light-emitting diodes from delayed fluorescence. *Nature*, **2012**, 492, 234 – 238. (*e*) Zhao, Z.; Deng, C.; Chen, S.; Lam, J.W.Y.; Qin, W.; Lu, P.; Wang, Z.; Kwok, H. S.; Ma, Y.; Qiu, H.; Tang, B. Z. Full emission color tuning in luminogens constructed from tetraphenylethene, benzo-2,1,3-thiadiazole and thiophene building blocks. *Chem.Commun.*, **2011**, 47, 8847 – 8849. (*f*) Park, Y. I.; Son, J. H.; Kang, J. S.; Kim, S. K.; Lee, J. H.; Park, J. W. Synthesis and electroluminescence properties of novel deep blue emitting 6,12-dihydro-diindeno[1,2-b;1′,2′-e]pyrazine derivatives. *Chem.Commun.*, **2008**, 2143 – 2145.

46.Hinoue, T.; Shigenoi, Y.; Sugino, M.; Mizobe, Y.; Hisaki, I.; Miyata, M.; Tohnai, N. Regulation of π-Stacked Anthracene Arrangement for Fluorescence Modulation of Organic Solid from Monomer to Excited Oligomer Emission. *Chem. Eur. J*. **2012**,18, 4634 – 4643.

47. Mizobe, Y.; Miyata , M.; Hisaki, I.; Hasegawa, Y.; N. Tohnai, N. Anomalous Anthracene Arrangement and Rare Excimer Emission in the Solid State: Transcription and Translation of Molecular Information. *Org. Lett.*, **2006**, 8, 4295 – 4298.

48. Zhang, G.; Yang, G.; Wang, S.; Chen, Q.; Ma, J. S. A Highly Fluorescent Anthracene-Containing Hybrid Material Exhibiting Tunable Blue–Green Emission Based on the Formation of an Unusual "T-Shaped" Excimer. *Chem. Eur. J.* 2007, **13**, 3630 – 3635.

49. Shen, Y.; Liu, H.; Zhang , S.; Gao, Y.; Li, B.; Yan, Y.; Hu, Y.; Zhao, Y.; Yang B. Discrete face-to-face stacking of anthracene inducing high-efficiency excimer fluorescence in solids via a thermally activated phase transition. *J. Mater. Chem. C*, **2017**, 5, 10061 – 10067.

50. "Chemistry of the Elements" Greenwood, N. N.; Earnshaw, E.A. 2nd Edition, Butterworth-Heinman, **1997**.

51. (a) Fu, X.-F.; Yue, Y.-F.; Guo, R.; Li, L.-L.; Sun, W.; Fang, C.-J.; Xu, C.-H.; Yan, C.-H. An enhanced fluorescence in a tunable face-to-face π···π stacking assembly directed by the H-bonding. *CrystEngComm*., **2009**, 11, 2268 – 2271. (b) Villapando, A.; Fronczek, F. R.; Isovitsch, R. The synthesis, X-ray structure analysis and photophysical characterization of 2-(9-anthrylmethylideneamino)- 5-methylphenol. *J.Chem.Cryst.*, **2011**, 41, 1342 – 1347.

52. Melen, R. L.; Less R.J.; Pask, C.M.; Rawson, J.M. Structural Studies of Perfluoroaryldiselenadiazolyl Radicals: Insights into Dithiadiazolyl Chemistry, *Inorg. Chem.*, **2016**, *55*, 11747 – 11759.

53. (a) Haleblian, J; McCrone, W. Pharmaceutical applications of polymorphism *J Pharm Sci.* **1969**, *58*, 911 – 929; (b) Bernstein J., Polymorphism in Molecular Crystals, Oxford University Press, 2002; (c) Nyman, J.; Day G. M. Static and lattice vibrational energy differences between polymorphs *CrystEngComm*. **2015**, *17*, 5154–5165.

54. Bernstein, J.; Davey, R.J.; Henck, J.-O. Concomitant polymorphs, *Angew. Chem. Int. Ed.*, **1999**, *38*, 3440 – 3461.

55. Kahn, O. Molecular Magnetism, VCH, Weinheim, **1993**.

56. (a) Fujita, W.; Awaga, K. Room-Temperature Magnetic Bistability in Organic Radical Crystals. *Science* **1999**, 286, 261 – 262. (b) Brusso, J. L.; Clements, O. P.; Haddon, R. C.; Itkis, M. E.; Leitch, A. A.; Oakley, R. T.; Reed, R. W.; Richardson, J. F. Bistability and the Phase Transition in 1,3,2-Dithiazolo[4,5-b]pyrazin-2-yl. *J. Am. Chem. Soc.*, **2004**, *126*, 14692 – 14693. (c) Brusso, J. L.; Clements, O. P.; Haddon, R. C.; Itkis, M. E.; Leitch, A. A.; Oakley, R. T.; Reed, R. W.; Richardson, J. F. Bistabilities in 1,3,2-Dithiazolyl Radicals. *J. Am. Chem. Soc.*, **2004**, 126, 8256 – 8265; (d) Alberola, A.; Collis, R. J.; Humphrey, S. M.; Less, R. J.; Rawson, J. M. Spin Transitions in a Dithiazolyl Radical: Preparation, Crystal Structures, and Magnetic Properties of 3-Cyanobenzo-1,3,2-dithiazolyl, $C_7H_3S_2N_2$. *Inorg. Chem.*, **2006**, 45, 1903–1905.

57. Mills, M.B.; Wohlhauser, T.; Stein, B.; Verdutn, W.R.; Song, E.; Dechambenoit, P.; Rouzieres, M.; Cleric, R.; Preuss, K.E. Magnetic Bistability in Crystalline Organic Radicals: The Interplay of H-bonding, Pancake Bonding, and Electrostatics in 4-(2′-Benzimidazolyl)-1,2,3,5-dithiadiazolyl, *J. Am. Chem. Soc*., **2018**, 140, 16904 – 16908.

58. Fatila, E. M.; Mayo, R. A.; Rouzières, M.; Jennings, M. C.; Dechambenoit, P.; Soldatov, D. V.; Mathonière, C. ; Clérac, R.; Coulon, C.; Preuss, K. E. Radical–Radical Recognition: Switchable Magnetic Properties and Re-entrant Behavior. *Chem. Mater.*, **2015**, 27, 4023 – 4032.

59. Suizu, R.; Iwasaki, A.; Shuku, Y.; Awaga, K. Spatially inhomogeneous, stepwise phase transitions in a thiazyl diradical: a structural mismatch induced by lattice transformation. *J. Mater. Chem. C*, **2015**, 3, 7968 – 7977.
60. Beldjoudi, Y.; Sun, R.; Arauzo, A.; Campo, J.; Less, R. J.; Rawson, J. M. Structural Variations in the Dithiadiazolyl Radicals *p*-ROC_6F_4CNSSN (R = Me, Et, ^{n}Pr, ^{n}Bu): A Case Study of Reversible and Irreversible Phase Transitions in *p*-$EtOC_6F_4CNSSN$. *Cryst. Growth Des.*, **2018**, 18, 179 – 188.
61. Cordes, A.W.; Haddon, R. C.; Hicks, R.G.; Oakley, R.T.; Palstra, T.T.M. Preparation and solid-state structures of (cyanophenyl)dithia- and (cyanophenyl)diselenadiazolyl radicals *Inorg. Chem*. **1992**, *31*, 1802 – 1808.
62 (a) Bucar, D.-K.; Lancaster, R.W.; Bernstein, J. Disappearing polymorphs revisited *Angew. Chem. Int. Ed.*, **2015**, *54*, 6972 – 6993; (b) Dunitz, J.D.; Bernstein, J. disappearing polymorphs *Accts. Chem. Res.*. **1995**, *28*, 193 – 200.
63. (a) Clarke, C. S.; Jornet-Somoza, J.; Mota, F.; Novoa, J. J.; Deumal, M. Origin of the Magnetic Bistability in Molecule-Based Magnets: A First-Principles Bottom-Up Study of the TTTA Crystal. *J. Am. Chem. Soc.* **2010**, 132, 17817 – 17830. (b) Vela, S.; Reardon, M.B.; Jakobsche, C.E.; Turnbull, M.M.; Ribas-Arino, J.; Novoa, J.J. Bistability in Organic Magnetic Materials: A Comparative Study of the Key Differences between Hysteretic and Non-hysteretic Spin Transitions in Dithiazolyl Radicals. *Chem Eur. J.*, **2017**, 23, 3479 – 3489. (c) Vela, S.; Mota, F.; Deumal, M.; Suizu, R.; Shuku, Y.; Mizuno, A.; Awaga, K.; Shiga, M.; Novoa, J. J.; Ribas-Arino, J. The key role of vibrational entropy in the phase transitions of dithiazolyl-based bistable magnetic materials. *Nature. Commun.*, **2014**, 5, 4411
64. Constantinides, C. P.; Carter, E.; Eisler, D.; Beldjoudi, Y.; Murphy, D. M.; Rawson, J. M. Effects of Halo-Substitution on 2′-Chloro-5′-halo-phenyl-1,2,3,5-dithiadiazolyl Radicals: A Crystallographic, Magnetic, and Electron Paramagnetic Resonance Case Study. *Cryst. Growth Des.*, **2017**, 17, 3017 – 3029.
65. Iwahara, H.; Kushida, T.; Yamaguchi, S. A planarized 9-phenylanthracene: a simple electron-donating building block for fluorescent materials. *Chem.Commun.*, **2016**, 52, 1124 – 1127.
66. Fehér, F. In *Handbook of Preparative Inorganic Chemistry*, 2nd ed., Vol. 1; Brauer, G., Ed.; Academic Press: New York, **1963**; p 371.
67. Bruker (**2008**). APEX2 (Version 2008.1-0). Bruker AXS Inc., Madison, Wisconsin, USA.
68. Bruker (**2001**). SAINT-V6.28A. Data Reduction Software.
69. Sheldrick, G.M. (**1996**). SADABS. Program for Empirical Absorption Correction. University of Gottingen, Germany.
70 Sheldrick, G.M. Crystal structure refinement with SHELXL, *Acta. Cryst. C.* **2015**, 71, 3 – 8.

Table of Contents: